VISUALIZATION AND EXPLORATION OF TIME-VARYING AND DIFFUSION TENSOR MEDICAL IMAGE DATA SETS

by

Zhe Fang

B.Sc. with Honours, Acadia University, 2003

A THESIS SUBMITTED IN PARTIAL FULFILLMENT
OF THE REQUIREMENTS FOR THE DEGREE OF
MASTER OF SCIENCE
in the School
of
Computing Science

SIMON FRASER UNIVERSITY
Spring 2008

APPROVAL

Name:	Zhe Fang
Degree:	Master of Science
Title of thesis:	Visualization and Exploration of Time-Varying and Diffusion Tensor Medical Image Data Sets
Examining Committee:	Dr. Greg Mori Chair
	Dr. Torsten Möller, Co-Senior Supervisor
	Dr. Ghassan Hamarneh, Co-Senior Supervisor
	Dr. Richard (Hao) Zhang, SFU Examiner

Date Approved: November 29, 2007

Abstract

In this work, we propose and compare several methods for the visualization and exploration of time-varying volumetric medical images based on the temporal characteristics of the data. The principle idea is to consider a time-varying data set as a 3D volume where each voxel contains a time-activity curve (TAC). We define and appraise three different TAC similarity measures. Based on these measures we introduce three methods to analyze and visualize time-varying data. The first method relates the whole data set to one template TAC and creates a 1D histogram. The second method extends the 1D histogram into a 2D histogram by taking the Euclidean distance between voxels into account. The third method does not rely on a template TAC but rather creates a 2D scatter plot of all TAC data points via multi-dimensional scaling. These methods allow the user to specify transfer functions on the 1D and 2D histograms and on the scatter plot, respectively. We validate these methods on synthetic dynamic Single Photon Emission Computed Tomography and Positron Emission Tomography data sets and a dynamic planar Gamma camera image of a patient. We use a similar idea to visualize diffusion tensor imaging. We will illustrate this visualization approach on a real patient data set. These techniques are designed to offer researchers and health care professionals a new tool to study time-varying and diffusion tensor medical imaging data sets.

Keywords: medical imaging; time-varying data; diffusion tensor MRI data; multi-dimensional scaling; volume rendering; transfer function

Subject Terms: medical visualization system; medical image processing; visualization data processing; computer graphics

To Mom, Dad and Brother!

"Well done is better than well said."

— Benjamin Franklin (1706 - 1790)

Acknowledgments

First of all, I thank both of my senior supervisors, Dr. Torsten Möller and Dr. Ghassan Hamarneh. This work would not have been possible without their consistent support and patient supervision. Their attitude towards research has greatly influenced me. This work benefited from their attentive reviews and technical expertise. I also thank Dr. Richard Zhang for his help during my studies at the GrUVi lab and serving as my thesis examiner.

Other members of the GrUVi lab provided their help and ideas, which made my studies at SFU very enjoyable. I thank all of my friends in Vancouver for making my life bright.

Finally, I am most thankful to my family for their continual support and encouragement throughout my studies in Canada. They are always there to help me, guide me and laugh with me.

Contents

List of Tables

List of Figures

Chapter 1

Introduction

1.1 Overview of Research

Computers have been widely used in health care during the past decade, from medical data storage to telematics, from data processing to treatment. Using computers in health care can improve the quality and effectiveness of care and reduce its cost.

While 3D medical imaging has become the standard in recent years for capturing structural information about anatomy, functional imaging studies, which additionally include temporal dynamics, are still on the forefront of medical imaging research. For example, dynamic Single Photon Emission Computed Tomography (SPECT), Positron Emission Tomography (PET), functional Magnetic Resonance Imaging (fMRI) and other modalities make it possible to trace changing distributions of radio labelled substances or examine magnetic phenomena associated with spatio-temporal brain activation. Physicians may use temporal in addition to 3-dimensional spatial information to diagnose pathological tissue based on its altered perfusion dynamics. They may track disease progress or its response to therapy over a short time or over several months or years. Further, they may examine correlations between diseases and drugs, and organ function. However, exploring and visualizing this multi-dimensional data remain challenging tasks.

For the purposes of this thesis, we consider time-varying 2D or 3D medical image data (TVMID). Using data from dynamic imaging alone, there is an inherent ambiguity in deciding whether the change in spatial location of activation is due to patient motion or due to a change in function of a stationary subject. Therefore, in any imaging acquisition, patients

are typically instructed to remain still or even hold their breath, whenever possible, during scanning. Alternatively data from other modalities (e.g. tracking devices or structural imaging) can be acquired and used to compensate for subject motion. There are alternative approaches and a huge body of literature dealing with motion correction and image registration. In this work, we make the assumption that volumes at different times are already spatially registered to each other and do not attend to this issue any further.

One way of understanding our time-varying image data is that each voxel, with coordinates (x, y) in 2D and (x, y, z) in 3D, does not contain a single scalar value any longer, as is common for the majority of 3D image data, but rather a temporal function, which is typically referred to as the Time-Activity Curve (TAC). This temporal behaviour is attributed to the interaction of tissue with a radioactive tracer (in SPECT and PET imaging) or the functional behaviour for fMRI. The source of this temporal behaviour varies with the particular modality. For example, in blood oxygen level-dependent fMRI, the captured data reflect the metabolic processes in the brain. Specifically, in active brain regions, blood oxygenation is higher than in resting regions. Since deoxygenated haemoglobin has a stronger reaction to the magnetic field than oxygenated haemoglobin, the temporal signals in fMRI at each voxel are indicative of brain activity. In dynamic SPECT, on the other hand, the recorded TACs are based on the detection of electromagnetic radiation, whose source is the injected radioactive pharmaceutical. Using a dedicated Gamma camera, photons are detected from different angles around the patient. The 2D information about their spatial distribution and the times they were detected is recorded. In a subsequent step, a series of 3D images corresponding to different times are reconstructed yielding a time-varying 3D image. Planar Gamma images from a single angle also provide useful functional information, even without subsequent 3D reconstruction. PET is somewhat similar to SPECT. However, instead of injecting the subject with gamma-emitting drugs, positron-emitting pharmaceuticals are used. Upon annihilation with electrons, these positrons emit two 511keV photons simultaneously in two opposite directions and a camera (with several rings of detectors) is used to record these signals arriving in coincidence from all directions.

Different regions of the body may exhibit different radio tracer uptake and washout, resulting in different temporal behaviour and related TACs. It is usually expected that all voxels corresponding to tissues with the same physiology, performing similar function, and/or belonging to the same healthy organ will display similar TACs. Nevertheless, there can exist voxels that are spatially close to each other but with very different TACs (e.g. at

boundaries of different organs). Vice versa, distant voxels can have very similar TACs (e.g. in the left and right lungs). As we will explain later, our proposed techniques allow the investigation and visual exploration of these scenarios.

More importantly, the altered physiology within an organ caused by disease may result in temporal behavior different from that of a healthy tissue. Recognizing abnormal behavior is important for the purpose of patient diagnosis [65]. However, it is not easy to discover such temporal changes and abnormalities in a TVMID by using conventional static segmentation or visualization tools designed for scalar fields. The basic motivation of this thesis is that detecting and quantifying the difference in the TACs allows the segmentation, quantification, and visualization of different organs or regions of interest.

Another part of this thesis work is related to the visualization of Diffusion Tensor Imaging (DTI) data. Diffusion is the movement by which molecules are transported from an area of high concentration to an area of low concentration. The diffusion-driven water molecules interact, bouncing or crossing, with many tissue components, which also probe tissue structure. DTI is a magnetic resonance imaging (MRI) technique used to measure the diffusion-driven displacements of water molecules at a microscopic scale. DTI is becoming increasingly valuable for assessing the effects of disease progression and treatment evaluation on fiber connectivity [63, 52, 77]. It is a challenge to visualize diffusion tensor data because of its multivariate nature. There is no single well established method to display a tensor field. One way to visualize DTI data is to contract each tensor to an appropriate scalar value or vector for a particular application by applying a carefully designed scalar metric in order to highlight useful information, for example the apparent diffusion coefficient (ADC), relative anisotropy (RA) and fractional anisotropy (FA), and then use available visualization software implementing standard algorithms, including volume rendering and iso-surface rendering. Another way to visualize DTI data is to use glyphs to represent each tensor. Both an ellipsoidal representation and an extended superquadrics approach [33] was proposed. Tractography, such as stream tubes [84], is another popular choice to visualize DTI. It is able to represent neural pathways by curves, which is hard to represent with discrete glyphs.

Similar to our TVMID visualization methods, we measure the similarity between tensors associated with voxels by a distance metric proposed by Wang and Vemuri et. al. [73]. Then, we use the direct volume rendering technique to visualize it. Our proposed work can therefore be regarded as a general framework for the visualization and analysis of 2D and 3D images with scalar, vector or tensor pixels, given an appropriate similarity metric

between the pixel values.

The primary objective of this work is to investigate new methods to visualize TVMID and to build an application which allows the user to easily explore these TAC-based data. One primary purpose of functional imaging is to distinguish diseased tissue from healthy tissue. Hence, in contrast to conventional time-varying visualization, where each time step is visualized separately, we consider all time steps at once and offer a comprehensive (non-animated) visualization of the time-behaviour. Visualizing each time-step separately does not provide comprehensive information about the dynamic profiles of different tissues and thus impairs the ability of researchers and health care professionals to perform an accurate and clear diagnosis.

1.2 Contributions

The main contributions of this thesis are:

- The interactive query of a particular dynamical tissue behaviour;
- The assessment of different distance metrics for the discrimination of tissue behavior;
- The assessment of the influence of the physical relationship of the TAC for the determination of different tissue behavior;
- Development of a framework and software system for the visualization of temporal behaviour of medical data; and
- Development of a visualization method for a DTMRI data set.

These visualization methods can be applied to most time-varying medical image data sets: dynamic PET, dynamic SPECT, planar dynamic single photon studies and fMRI. We show the effectiveness of our visualization methods on dynamic SPECT and PET data sets created by using physical or computational phantoms as well as on a dynamic planar Gamma camera image of a patient. We believe that visualizing the TVMID by our new methods is intuitive, provides new insight into these types of data sets and, consequently, helps improve diagnosis and treatment evaluation.

1.3 Thesis Organization

Chapter 2 introduces the different time-varying medical signal acquisition methods. Chapter 3 surveys time-varying volumetric data visualization, time-varying medical data segmentation and multidimensional scaling. Chapter 4 describes our time-varying medical data sets visualization methods. Chapter 5 describes our visualization system and results. Chapter 6 describes our attempt to extend the time-varying medical data visualization work to diffusion tensor magnetic resonance images. Chapter 7 discusses the research and contribution of our work. Chapter 8 proposes some future work.

Chapter 2

Time-Varying Biological Signals and Medical Images

Throughout the lifetime of all living things, organisms generate various signals, which reveal the properties of tissue, organ or cell systems. These signals can be electrical or non-electrical signals. Modern technologies allow us to measure, record and analyze these biological signals. *Medical imaging* techniques can generate images of the human body. These images will help doctors to make clinical decisions or researchers to study anatomical structure or functionality. Some techniques, such as electrocardiographs and electroencephalograms and others, do not generate images but maps of a body's potential information instead. These techniques could be included as certain forms of medical imaging.

Image reconstruction techniques could produce 3D images of patients. For example, in *Computer Tomography (CT)*, a narrow X-ray beam passes through the patient's body. The combination of an X-ray tube and a detector is used to measure the attenuation of a beam through the patient's body. Attenuated beams result in pixels on the two-dimensional images and indicate how strongly the incident beam passing through that position was attenuated by the patient's tissue. Since a single pixel was due to an attenuation medium that was present over the whole beam path, we cannot determine where along the path the attenuation occurred. Therefore, the same procedure is repeated from different angles, which results in many images of the same area. If enough images are acquired, it is possible to compute the accurate attenuation property per voxel in the area. The attenuation coefficient is characteristic for the chemical composition of the tissue. The technique explained above

is called 3D reconstruction and can be achieved via the filtered back projection algorithm, which is the most frequently used technique in CT to obtain the attenuation. SPECT can also use the back-projection technique at the reconstruction stage.

Recently, techniques have been developed to enable scanning software to produce both three-dimensional spatial anatomical structure and corresponding temporal functional information for the physician. Temporal information provides insight into disease and plays an important role in health care. The changes in a patient's disease may occur over many years. The evolution and treatment of disease is also a process over time. In the following sections, we will introduce different modalities which can be used to acquire temporal related *bio-signal* and *medical images.*

2.1 One Dimensional Spatial and Temporal Bio-signals

Electrocardiography is widely used to record the electric activity of the heart over time. The cardiac muscle generates an electric field on the body surface. The electric potential maxima and minima increase and decrease during each cardiac cycle. The recording of this electric potential as a function of time is an *electrocardiogram (ECG).* During the measurement, up to 12 self-adhesive electrodes are attached to select locations on the skin of the arms, legs and chest. The information obtained from an ECG is important for diagnostic purposes such as discovering different types of heart disease. It is useful for evaluating how well the patient is responding to a certain drug or to devices used to regulate the heart.

An *electroencephalogram (EEG)* is a test that measures and records the electrical activity of the brain by using electrodes attached to the scalp and connected by wires to a computer. The computer records the brain's electrical activity on the screen or on paper as wavy lines. These lines represent the electrical signal from a large number of neurons. *EEGs* are routinely recorded and interpreted in neurology and neurophysiology because the process is non-invasive to the research subject. It is one of few high temporal resolution techniques that is capable of detecting changes in electrical activity in the brain on a millisecond-level. Frequency analysis is typically applied to *EEGs* before clinical usage. A series of band-pass filters or Fourier analysis, for instance, is often applied in order to reveal interesting parameters of an *EEG. EEG* is often used to help diagnose and evaluate certain clinical situations, such as sleep disorders, head injury and coma.

An *electromyogram (EMG)* is a test that is used to record the electrical activity of muscles. An electromyograph detects the electrical potential generated by muscle cells when these cells contract and relax. *EMGs* can be used to detect abnormal muscle electrical activity that can occur during many diseases and conditions, for instance, muscular dystrophy (inflammation of muscles).

An *electrooculograph* is a technique for measuring the difference in electrical charge between the front and back of the eye that is correlated with eyeball movement (as in REM sleep). The resulting signal is called the *electrooculogram (EOG)*. It is obtained by electrodes placed on the skin near the eye.

Magnetoencephalography (MEG) is an imaging technique used to measure the magnetic fields produced by electrical activity in the brain via extremely sensitive devices. *MEG* is a completely non-invasive technology for functional brain mapping and provides excellent temporal resolution. These measurements are commonly used in both research and clinical settings. There are many uses for *MEG*, including assisting surgeons in localizing a pathology, assisting researchers in determining the function of various parts of the brain, neuro-feedback, and others.

ECG, EEG, EMG, EOG and *MEG* are one-dimensional temporal signals (or multiple one-dimensional signals measured at different locations), as opposed to other modalities, e.g. ultrasound, which generate two- and three-dimensional temporal images, as well as *PET* which results in three-dimensional temporal images, as explained in the following section.

2.2 Two and Three Dimensional Spatial and Temporal Biosignals

Medical imaging techniques are widely used as tools to non-invasively examine the human body. From the insight provided by medical images, doctors and researchers can improve their understanding of the patient's body, examine disease and make better diagnostic decisions. Since Röntgen discovered the X-ray in 1895, different medical imaging modalities have been invented for various medical purposes. The pipeline of information extraction from medical images usually consists of six stages (See Figure 2.1.) :

1. The physical properties of a patient are acquired by different medical imaging devices,

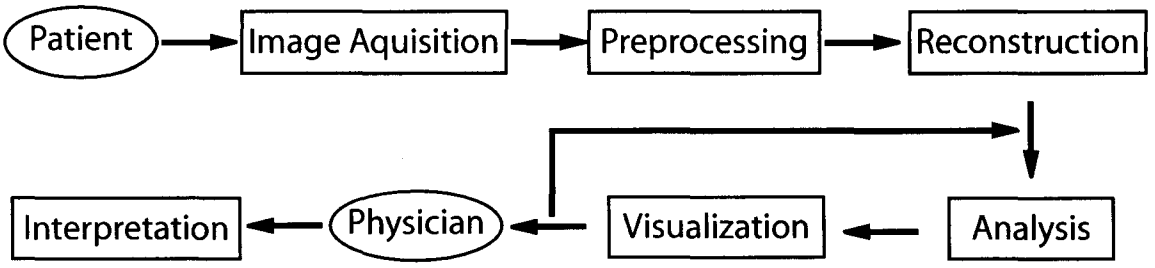

Figure 2.1: The six stages of information extraction from medical images.

such as CT, MRI or ultrasound at the data *acquisition* stage.

2. Some techniques, such as de-noising and contrast enhancement, are applied in order to enhance the acquired raw data during the *preprocessing* stage.

3. The preprocessed data are *reconstructed* to physically meaningful images or volumes.

4. Reconstructed images or volumes are typically *processed* and *analyzed* in order to highlight the important information. For example, image segmentation and registration can be used.

5. The information from the previous stage is rendered on the two-dimensional plane of a graphic monitor at the *visualization* stage. Analysis and visualization may be interchanged since the result of visualization may be useful in providing better analysis, especially in user-guided image analysis.

6. Combining data with professional knowledge, the physician can make certain *interpretations* and decisions.

The image that results directly from the data acquisition stage shows degradation caused by various processes. It is important to reverse some degradation in the image at the preprocessing stage for further processing or visual inspection. The a priori knowledge is important during this inverse process. For example, knowledge about the nature of the degradation and the properties of the data acquisition device and the nature of noise will help correct some degradation. The techniques used at the preprocessing stage are applied, with various goals. They may operate globally or locally, in the frequency or spatial domain.

The resulting images from the previous step are two-dimensional projections, which utilize the measurement of radiation in the patient's body from a large number of angles.

In order to get the three-dimensional distribution of activity, a reconstruction algorithm should be applied. The filtered back projection algorithm and its variants are often used because of its efficiency.

In some applications, the reconstructed images or volumes are to be analyzed or processed; for example, they can be segmented into different components or registered together at the same possible region. Image segmentation is a process that decomposes an image into several constituent components. Then, different measurement can be performed on interesting components. Several approaches are used to segment intensity images or volumes. One approach is based on the analysis of the histogram of intensity values. Another approach uses region based methods. Several initial points are placed in the regions to be detected. A neighbouring pixel is assigned in the initial region if it has a similar intensity level. This process is continued until all pixels in the image have been assigned. Image registration is the process of finding the one to one correspondence between two images of the same scene. When two or more images are acquired at different times, in order to detect possible changes of the same scene, they need to be aligned. Medical image registration can also be used to register the patient's data to an anatomical atlas.

With the introduction of medical image modalities (CT, MRI, PET and fMRI), enabling three-dimensional anatomical information or even four-dimensional functional information to be acquired, many visualization methods have been developed to help improve our understanding of these modalities. Traditionally, a doctor needs to form a mental image of a patient's structures by looking at the acquired images slice by slice. This is a difficult and time consuming process. The accuracy of the acquisition device improves dramatically, resulting in more and more image slices, making it take longer to make diagnostic decisions in a traditional way. Medical visualization can help overcome this problem by presenting the reconstructed data sets from a set of image slices. Regions of interest can be highlighted.

Different medical image modalities are discussed in the following sections.

2.2.1 SPECT and Dynamic SPECT

Single photon emission computed tomography (SPECT) is an emission tomography technique which measures the physiological functions in tissues. Before imaging, a patient is administered radiopharmaceuticals labeled with a single-photon emitter, which emits one gamma-ray photon with each radioactive decay event [76]. A gamma camera rotates around the patient to acquire several 2D images from different angles. The 2D images show the

radioactive tracer distribution from different angles. A reconstruction algorithm, e.g. filtered back projection, can be applied to reconstruct the three-dimensional volume of the radioactive tracer distribution within the patient. Several gamma cameras may be used simultaneously in order to accelerate the acquisition. During the scanning, the patient should remain still. Movement will degrade the quality of the reconstructed images. Some reconstruction techniques can help compensate for movement. When using SPECT to scan the heart, which moves repetitively, an ECG machine can be used to record the different stages of its contraction cycle simultaneously. This technique is called *gated SPECT imaging.*

Dynamic single photon emission computed tomography (dSPECT) is an emission tomography technique which could provide functional dynamic information of the body. Compared with *SPECT*, which can only acquire the spatial location of tracer molecules, *dSPECT* can acquire both temporal and 3-dimensional spatial information of activity distribution in the patient. Some research groups, such as the Medical Imaging Research Group (MIRG) at University of British Columbia (UBC), are investigating the possibility of acquiring dSPECT data by using conventional clinical equipment and data acquisition protocols [25].

In *SPECT*, it is commonly assumed that the properties of the patient's internal organs do not change during the time of measurement. It is a conventional diagnostic tool to measure the stationary activity distribution. The relatively long acquisition times and short half life of the radioactive tracers make it difficult to acquire clear static SPECT images [7]. *dSPECT* is designed to provide both temporal and spatial information. The temporal information, which provides the changes in activity distribution in the body, could potentially enhance diagnosis and research. The filtered back projection method cannot be applied to the reconstruction of *dSPECT* data, because it may cause artifacts or even wrong results. Reconstruction methods are discussed in [7], which consider the measurement system as a linear system. The result of *dSPECT* reconstruction is a time-series of 3-dimensional *SPECT* images, which represent the tracer distribution at each particular time step.

2.2.2 PET

Positron emission tomography (PET) is a nuclear medicine imaging technique used to provide functional information. It is a non-invasive imaging technique, but patients are exposed to a small dose of radiation.

The main difference between *PET* and *SPECT* is that *PET* uses radiopharmaceuticals labeled with a positron-emitting isotope and *SPECT* uses single-photon emitters. The decay

of each nucleus of the positron-emitting isotope emits a positron. The positron quickly annihilates with an electron and then produces two gamma photons, which move in nearly opposite directions from one another. Each gamma photon has 511keV energy.

The patient is surrounded by rings of gamma-ray detectors in the *PET* scanner. The detectors are connected to sensors in order to record the time of the gamma-ray detection [76]. If two gamma rays are detected almost at the same time, it is most likely that they are generated from the same decay event. The position where the decay event happened is then calculated.

The *PET* scanner can only provide metabolic information about the body. It is more useful to combine anatomic information with metabolic information. Modern *PET* scanners are usually integrated with *CT* scanners in order to provide anatomical imaging. After sequential scans by *PET* and *CT*, the two sets of images are fused together precisely by registration [66]. The anatomic structure and undergoing biochemical activity are presented simultaneously.

2.2.3 Magnetic Resonance Imaging

Magnetic Resonance Imaging (MRI) is a non-invasive technique for providing an image of the tissue distribution in the body. Because electromagnetic (EM) waves and a strong magnetic field are used (instead of ionizing radiation or x-ray) in producing an MRI image, there is no known radiation risk to the patient at low magnetic field strength (e.g. 1 or 3 Teslas).

Hydrogen nuclei (protons) have spin and behave like small magnets. Under normal circumstances, the protons within a human body randomly point in all directions and the magnetization of the body is canceled out. When a strong magnetic field is applied to the body, protons align either parallel or anti-parallel to the magnetic field. Pulses of electromagnetic radiation are then applied to stimulate the magnetic protons. When the electromagnetic radiation is perpendicular to the external magnetic field and has a certain frequency, called the Larmor frequency, the protons precess around the direction of the external field. The Larmor resonance frequency of the hydrogen nucleus is different at different locations of the body. It is proportional to the external magnetic field. By applying different frequencies of electromagnetic radiation, MRI can produce a density image of the hydrogen nuclei in the body.

Compared to CT, which provides a good image of dense tissue such as bone, MRI is able

to generate clearer pictures of soft tissue. Therefore, MRI is widely used to diagnose joint injuries and examine organs of the chest and abdomen. This type of imaging, including T_1, T_2 and PD MRI, produces scalar 3D images.

Functional magnetic resonance imaging (fMRI) is a neuro-imaging technique for mapping changes of the brain activity caused by different types of stimuli, such as sound and pictures. It is a non-invasive scan and uses a MRI scanner with parameters sensitive to changes in magnetic susceptibility. The change in magnetic susceptibility is caused by a change of the level of oxygenation of venous blood or a change in the rate of in-flowing arterial blood. The activated brain regions are where the level of oxygenation and the rate of blood flow is greater than in resting regions. The magnetic resonance signal of the blood is therefore slightly different depending on the level of oxygenation.

During the *fMRI* scanning procedure, the subject is presented with a particular form of stimulation. Then, MRI images of the patient's brain are taken and are used to provide high resolution anatomical information after reconstruction. Next, a series of images related to the temporal response of the blood supply is taken over time. These images provide low resolution temporal information. Some research groups are trying to combine *fMRI* with *EEG* and *MEG* in order to provide high resolution temporal information. The image data produced with *fMRI* contains both 3-dimensional spatial anatomical information and temporal information. It is then analyzed to produce statistical maps (scalar images) that convey the confidence region activation that correlates with the stimulus. *fMRI* makes it possible to examine magnetic phenomena associated with spatio-temporal brain activation. Physicians may use temporal in addition to 3-dimensional spatial information to diagnose pathological tissue based on their altered perfusion dynamics.

Perfusion magnetic resonance imaging (perfusion MRI) is a non-invasive technique to detect flow within vessels and is sensitive to microscopic levels of blood flow. Perfusion is a process in which the blood flows through the blood vessels. Compared with PET and SPECT, which can also measure the perfusion, MRI provides higher spatial and temporal resolution.

Tagged magnetic resonance imaging (tagged MRI) is an imaging technique to estimate the displacement field for all points within a certain organ. Tagging is the magnetic resonance process of using special pulse sequences to impose temporary spatial variations in the longitudinal magnetization of protons inside the body. The temporary spatial variations are called tags. Tags move with underlying tissue in subsequent images, which aids in tracking

motion of objects using a series of magnetic resonance images. The tagged MRI has been used to track normal and abnormal myocardial motion and to understand the effects of treatment after myocardial infarction [31].

Diffusion tensor magnetic resonance imaging (DTMRI) is an extension of diffusion MRI, which applies diffusion gradients in at least six non-collinear directions. DTMRI measures the preferentially oriented diffusion or anisotropic diffusion. Anisotropic diffusion has been used to measure the structural integrity of brain white matter at different ages and in several diseases [34]. The direction of greatest diffusion has been used as the direction of white matter nerve fiber tracts.

MRI is a noninvasive and versatile medical imaging technique. In addition to acquiring a scalar image, TVMID, such as perfusion MRI and tagged MRI can also be obtained. DTMRI can also generate tensor fields.

2.2.4 Time-Varying Ultrasound

Medical ultrasound imaging, also called ultrasonography, is a technique that uses high frequency sound waves to generate images of the patient's body. It is a non-invasive and radiation-free technique, which is often used to scan pregnant women in order to evaluate the fetus. In an ultrasound scanner, pulsed sound waves are first generated with frequencies much higher than audible sound. The sound waves are absorbed, scattered or reflected by the patient's body. Most of the energy is reflected and causes strong echos. The energies and arrival times of the echos are measured. The distance between ultrasound source and reflectors is then calculated by the time intervals between the emission of the sound wave pulse and the arrival times of the reflected echos. The recorded waves can generate two-dimensional gray-scale images of the human body. The energy of the reflected ultrasound wave can be displayed as a one-dimensional plot (energy v.s. time). When the speed of sound in the tissue is known the time axes can be replaced with the distance. When the ultrasound is moved or there is an array of transducers, many such curves can be generated for physically adjacent paths in space. These multiple curves can be represented as rows or columns of a 2D image, with brightness proportional to energy. In 2D time-varying ultrasound, the whole process is repeated with time. Traditional 2D ultrasound images are grainy-looking and require the interpretation of a skillful technician.

Three-dimensional ultrasound is acquired by an ultrasound scanner. The acquired data is the distribution of ultrasonic echo information in 3D space, stored in memory as a 3D

array. Different from regular MRI or CT reconstructed 3D volumes, one can imagine the 3D ultrasound volume as a cone. 3D time-varying ultrasound is acquired in both three spatial dimensions and in the temporal dimension. 3D time-varying ultrasound takes a series of 3D ultrasound images and produces a live video.

Chapter 3

Related Work

In this section, we review techniques for visualizing time-varying volumetric datasets, previous work on segmenting time-varying medical data and multidimensional scaling, and describe how our work differs from other studies of time-varying medical image data set visualization.

3.1 Time-Varying Volumetric Data Visualization

The rendering community thus far has mostly focused on the technical aspects (accuracy and speed) of rendering very large data sets. This problem has been elevated by time-varying data, since many data structures cannot easily be updated from one time frame to the next in real-time. It requires reading large files continuously during the visualization process, which prevents visualization at interactive rates.

Generally, previous research on time-varying data visualization methods can be divided into three categories:

- Encoding/Compression,
- Feature extraction, and
- Rendering.

There are two types of time-varying volume dataset compression methods: value-based encoding and physically based feature extraction methods. Value-based encoding methods

transform (and potentially compress) data by exploiting coherence. The value-based encoding/compression [27, 42, 41, 59] methods could reduce the size of the datasets and therefore make storage more manageable. Exploiting coherence is the key to value-based encoding methods. Data features [61, 57, 54], such as vortices or shocks, can also be represented in a compact fashion. The data can be represented as a set of features instead of just a collection of voxels, which provides a higher level view of the data. Woodring et al. [81] proposed an approach which computes projections from a 4D to a 3D hyperplane by considering time-varying volumetric data as a four-dimensional data field. The 3D hyperplane projections are visualized by volume rendering.

Depending on the discrepancy between time steps, one can also classify the time-varying visualization as

- Homogeneous, or
- Inhomogeneous.

In other words, one can treat time-varying data sets either as 4D data [81, 41] or separate the temporal dimension from the spatial dimensions [59].

Several data structures or encoding methods have been proposed to accelerate the rendering time, such as T-BON [64], time-space partition trees [59], differential time-histogram tables [83] and others.

The temporal branch-on-need tree (T-BON) is an isosurface extraction data structure for time-varying data sets. It is an extension of three-dimensional branch-on-need octree (BONO) [78] to time-varying data sets. Instead of reading the entire tree and data from disk at each time step, T-BON improves the I/O performance by only reading the portion of the data necessary to construct the isosurface of the current time step. The geometry-based tree structure can also help to explore spatial coherence and therefore increase the performance.

The time-space partition (TSP) tree is a time-supplemented octree, which treats spatial and temporal dimensions equally. This is a data structure proposed to accelerate the volume rendering of time-varying data sets. The user is able to control the trade off between image-quality and rendering-speed by providing different error tolerances [59].

The differential time-histogram table (DTHT) is a data structure which encodes the temporal coherence and histogram distribution of time-varying data sets. DTHT is used to

reduce the data loaded from disk between adjacent time steps by a given error tolerance. Further, spatial distribution is also used to accelerate rendering [83].

Ma et al. [44] give a survey of different time-varying data visualization techniques. The survey focuses on how time-varying volume data can be efficiently rendered to achieve interactive frame rates by employing data encoding, hardware acceleration, and parallel pipelined rendering. The motivation for most of this research is rooted in massive data volumes, which are common in engineering problems. (See, for example, the Richtmeyer-Meshkov data [48].) Many time-varying data sets are typically produced by simulations of some complex physical phenomena. The ability to understand complex phenomena is important to solve many engineering problems. Most time-varying datasets are directly rendered as an animation sequence which shows how the underlying structures change over time.

However, the goal of medical diagnosis is not to observe a time-behaviour as much as to differentiate healthy from malicious tissue. Hence, it is not so important to provide an interactive selection of arbitrary time-slices, but rather a comprehensive evaluation of the time-behaviour of each tissue sample and its classification into different tissue types and tissue behaviours. Therefore, novel transfer function designs that take the whole data set into account are needed.

Recently, several approaches have been proposed to extend the aspect of transfer function design to time-varying data in a comprehensive way [3, 21]. A time histogram is given by concatenating a series of conventional 1D histograms together for each step. Hiroshi et al. [3] present a visualization method based on the time histogram, which allows simultaneous classification of the entire time series. In their system, the user can specify transfer functions either directly or indirectly using the time histogram and achieve interactive feedback.

Jankun-Kelly and Ma [30] study transfer function generation for time-varying volumetric data sets. They assign a single or a small set of transfer functions to an entire time series in order to capture dynamic behavior. The criteria are discussed when more than one transfer function is used. The transfer function for the entire time series is based on given transfer functions for each time step.

Tzeng and Ma [71] present a new time-varying data visualization system by employing machine learning. Machine learning algorithms are used to "learn" to extract and track features in time-varying flow field data sets. A transfer function for the entire time series is given by transfer functions from a few key time steps.

The approach taken in this thesis is to treat each voxel as a time-activity curve (TAC), as opposed to reducing it to a scalar. We then simply try to cluster these functions in groups with similar behaviour, creating a 1D or 2D transfer function. We then specify the regions of interest using an interface similar to that described by Doleisch et al. [22]. However, in our case the 2D space in which we specify the regions of interest is obtained by using a clustered representation provided via multidimensional scaling (MDS) [79].

Tory et al. [67] discuss several methods to visualize specifically time-varying medical data. They explore visualization methods, which include isosurfaces, direct volume rendering and vector visualization using glyphs, to produce an animation of consecutive time steps that illustrate how the intensity and gradient changes along the time. They argue that these visualization techniques could provide new insight into the information contained in the TVMID and therefore help improve diagnosis or treatment. However, their system is not capable of classifying data into different tissue types.

3.2 Segmentation of time-varying medical data

Our proposed framework allows for identification and visualization of regions with particular dynamic behaviour. Several techniques have been proposed in the past for the segmentation of time-varying medical image data. What is characteristic about these techniques is that once the 3D+time image data, along with some initial parameters, are set, the user has no influence over the segmentation outcome. Our framework, on the other hand, provides the user with the means to intervene, by leveraging their domain specific expertise. This is accomplished via an intuitive graphical interface while providing immediate visual feedback of alternative segmentation results. This keeps the clinical expert in the loop, which guarantees producing accurate and meaningful results.

A majority of previous "black-box"-type segmentation techniques is based on clustering [1]. In [80], a k-means like algorithm is used to cluster PET images, whereas in [2] fuzzy c-means (FCM) clustering is used to segment SPECT images. Velamuru et al. [72] used hierarchical clustering as well as inter- and intra-cluster measures to assess tissue activity. In [26], pre-clustering and hierarchical clustering are used with extracted kinetic parameters to label PET data.

Our approach is based on reducing the dimensionality of the data by embedding the

TACs of all the voxels in a two dimensional space. The separation between the TAC observations in 2D is proportional to the measure of TAC dissimilarity. Effectively this iteratively groups the TAC observations while continuously producing an update of the 2D view. Toennies et al [65] discuss a dynamic SPECT segmentation scheme for aggregating voxels with similar TACs by using principal component analysis (PCA). The similarity of voxels is measured on the most significant components of the transformation of TACs in eigenspace, in order to bring the signal-to-noise ratio to a level which would improve the diagnostic potential. In [36], FCM is compared to other techniques based on expectation-maximization (EM) and independent component analysis (ICA). The use of ICA is somewhat related to our approach as both perform dimensionality reduction. Other previous work incorporated spatial information in clustering PET data through Markov Random Fields (MRF) [20, 39]. In our framework, the geometric distance between TACs can be taken into account during the dimensionality reduction and clustering and the user can visualize, on the fly, the results of interactively changing the degree of influence of spatial TAC proximity on the final segmentation.

Other approaches for segmenting time-varying medical images are based on energy minimization of a 3D+time explicit, parametric deformable model and are typically applied to dynamic cardiac data [46, 49], and tagged cardiac MRI data [47]. Implicit, level-set based deformable models have also been proposed more recently to segment time varying medical image data [35]. Deformable registration-based segmentation has also been proposed to address 3D+time segmentation. Here, a labelled initial 3D volume is provided and then non-rigidly deformed to subsequent time frames in order to transfer the labels throughout all volumes [18]. In a more recent work, Song et al. [62], combine segmentation and registration for dynamic renal MR images. These deformable shape model based techniques have been generally designed for modalities that exhibit a non rigidly varying shape over time, rather than stationary anatomy that exhibits dynamic activity, which is the main focus of our work. Analyzing functional MRI data provides a somewhat unique perspective. The data is typically reduced to scalar statistical parametric maps based on confidence values of activation and then simple thresholding is applied to highlight regions of interest [24].

3.3 Dimensionality Reduction

Dimension reduction is the process of reducing the number of dimensions under consideration, which allows us to visualize, categorize, interpret or simplify large datasets. It can be divided into

- Feature selection, and
- Feature extraction.

Feature selection approaches try to choose a subset of the original dataset and some data analysis which conducted in the reduced dataset will be more accurate than in the original one. Feature extraction is a mapping procedure from original multidimensional space into a space with fewer dimensions. In either approaches, the goal is to find a lower dimensional representation of the data that preserves most of the information or structure in the data.

The mapping procedure of feature extraction can be done either linearly or nonlinearly. Within the realm of linear feature extraction, two techniques are commonly used: principal components analysis (PCA) [8] and Fisher's linear discriminant (LDA) [40]. PCA performs a linear mapping of the data to a lower dimensional space such that the variance of the data in the lower dimensional space is maximized. LDA performs dimensionality reduction while preserving as much of the class discriminatory information as possible. Nonlinear dimensionality reduction performs nonlinear mapping from the high dimensional space to the low dimensional non-linear manifold. Kernel PCA methods employ PCA in a nonlinear way by means of a kernel trick. The isomap method estimates the distance between two points on a manifold by following a chain of points with shorter distances between them in order to retain global properties of the data. Other nonlinear methods, such as locally linear embeddings (LLE), only represents the distance between local points. A completely different approach to nonlinear dimensionality reduction is through the use of autoencoders, such as MDS and Sammon mappings [55]. Our approach applies the MDS method to reduce the dimensionality of the data by embedding the TACs of all the voxels in a two dimensional space. We will discuss the detail of the MDS method in the following paragraphs.

MDS is a dimensionality reduction technique, which maps high dimensional data points down to a lower dimensional embedding. During the dimensionality reduction process, the low-dimensional layout tries to best preserve the inter-point distances in the higher dimensional data. Classical MDS starts with a distance matrix of item-item similarities

[13]. The eigenvectors of the distance matrix are then computed and all items are projected onto a low-dimensional basis vector which preserves the highest amount of variance. The cost of solving the distance matrix for eigenvectors is $O(n^3)$. Later, Chalmers [17] proposed a physically based model which computes the distance between two small sets of items and gradually adjusts the position of items after each iteration. Each iteration produces good layout by applying stochastically-based algorithm with linear complexity. Depending on the size of the dataset, the overall cost of this approach is $O(n^2)$.

MDS is well suited to the task and well studied in database applications and visualization [6, 50, 51]. However the size of our data is unprecedented for such algorithms. (Our data may have more than one million data points.) A fast and interactive MDS system would help the user easily explore the data sets interactively. Hence, we employ the MDSteer [79] system, a steerable mass-spring model MDS system.

MDSteer is both a steerable MDS computation engine and a visualization tool, which progressively lays out points in the dataset. The algorithm iteratively alternates between the layout stage and the binning stage. During the layout stage, the algorithm iterates on the activated points, a sub-set of points in the dataset, in order to calculate the position on the projected plane. During the binning stage, the rectangular screen-space region is hierarchically decomposed into sub-regions. Each sub-region is called a bin, which is drawn as a wireframe box on the screen. The user can select some bins in order to reallocate available computational resources to focus on the "filling in" of those bins.

Chapter 4

Methods

In order to understand, analyze, and render the TAC volume, we need to define operations on these TACs that will enable us to use standard volume rendering tools common for 3D scalar data. Additionally, in order to be able to assign colour and opacity to a particular TAC, we need to adapt classical scalar field based transfer functions to time-varying data. One of the key ideas of transfer function design is to select a particular feature (i.e. iso-value for scalar volumes) and assign it a particular colour and opacity. Then, typically, voxels with similar feature values are assigned a slightly smaller opacity. (See Levoy [38].) The same principle can be applied to arbitrary data, including TAC-based data, as long as the notion of *similarity* is well defined. Hence, the key is the definition of a distance metric among TACs.

The general approach of our work is to define a distance metric for the space of TACs. (See Section 4.1.) Given a particular distance metric there are two principle ways to explore the TVMID. The user can either select a voxel (and hence its TAC) interactively or can input an arbitrary TAC into the system. Our system will then render all TACs that are within a particular distance of the desired TAC. (See Section 4.2 and Section 4.3.) As an alternative, the distances from each TAC to all other TACs in the volume can be computed. We then apply multi-dimensional scaling (MDS) to lay out this high-dimensional graph of all TACs on a 2D palette that is the basis of interactive exploration of the underlying TVMID. (See Section 4.4.)

4.1 Similarity measures for TACs

For traditional 3D (static) data our volume V_s is a scalar volume, i.e. $V_s : \mathbb{R}^3 \rightarrow \mathbb{R}$. However, in this paper we deal with a dynamic volume V_d defined as $V_d : \mathbb{R}^3 \rightarrow C^0(\mathbb{R})$. Here $C^0(\mathbb{R})$ is the space of all continuous functions. (This differs from the traditional approach $V_t : \mathbb{R}^4 \rightarrow \mathbb{R}$.) This representation is not unreasonable, since the change of activity concentration observed in the tissue will be gradual. The possibility for distance measures on the spaces $\mathbb{R}$ as well as $C^0(\mathbb{R})$ include the L_p metric, of which we will use the L_1 as well as L_2 metrics:

$$d_1(v_i, v_j) = \int_{-\infty}^{\infty} |v_i(t) - v_j(t)| dt \tag{4.1}$$

$$d_2(v_i, v_j) = \sqrt{\int_{-\infty}^{\infty} (v_i(t) - v_j(t))^2 dt} \tag{4.2}$$

where $v_i, v_j \in C^0(\mathbb{R})$, i.e. they are image TACs, which are functions over time.

Assuming we have N time samples, the discretized version of L_1 and L_2 (denoted by l_1 and l_2) are given by

$$d_1(v_i, v_j) = \frac{1}{N} \sum_{n=1}^{N} |v_i[t_n] - v_j[t_n]| \tag{4.3}$$

$$d_2(v_i, v_j) = \sqrt{\frac{1}{N} \sum_{n=1}^{N} (v_i[t_n] - v_j[t_n])^2} \tag{4.4}$$

Further, we consider the cross-correlation between two signals, which is given by:

$$v_i \star v_j(t) = \int_{-\infty}^{\infty} v_i(\tau) v_j(\tau + t) d\tau \tag{4.5}$$

For the purposes of defining a *similarity* measure, we can consider the maximum cross-correlation, i.e.

$$s_C(v_i, v_j) = \max_t \int_{-\infty}^{\infty} v_i(\tau) v_j(\tau + t) d\tau \tag{4.6}$$

Again, in its discretized version we have:

$$s_C(v_i, v_j) = \max_k (\frac{1}{N} \sum_{n=1}^{N} v_i[t_n] v_j[t_n + k]) \tag{4.7}$$

where $k \in \mathcal{Z}$ and $v[k] = 0$ for $k \notin [0, N]$.

Last, but not least, the Euclidean distance between voxels will also play an important role in the classification of the tissue. Hence, in a slight abuse of our notation, we will also define the Euclidean metric as

$$d_E(v_i, v_j) = \sqrt{(x_i - x_j)^2 + (y_i - y_j)^2 + (z_i - z_j)^2} \tag{4.8}$$

where (x_i, y_i, z_i) and (x_j, y_j, z_j) are the spatial locations of v_i and v_j respectively.

4.2 Distance to Template TAC One-Dimensional Histogram

As in scalar volume visualization, where features are typically specified as a particular iso-surface value, we can similarly determine a particular template TAC. Such a template TAC can be determined by interactively probing the underlying data (by specifying an arbitrary voxel via its spatial location (x_k, y_k, z_k)) or by simply sketching a template TAC. Often the clinician knows or expects a particular temporal behaviour from a particular tissue. Hence the a priori specification of a template TAC is a valuable feature of our system.

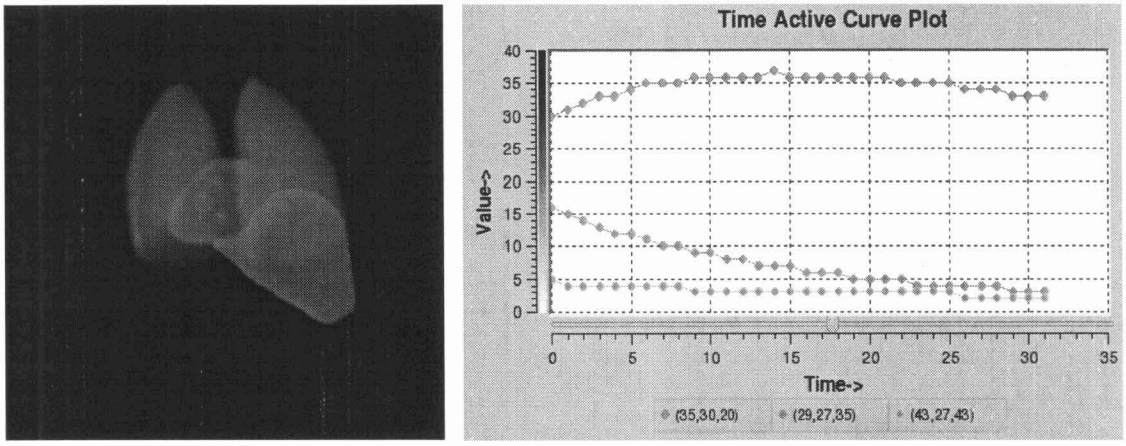

(a) (b)

Figure 4.1: The time activity curve visualization and design interface. (a) Volume rendering of distance volume using the d_1 distance between each TAC with the template TAC. The template TAC used was a TAC from the heart (green). (b) Representative time activity curves corresponding to the volume view for lungs (blue), heart (green), and liver (red). The position of corresponding voxel is shown at the bottom.

Figure 4.1 shows the widget we created for the inspection and modification of TACs. While Figure 4.1a shows the volume rendered result of some classification of a phantom data

set, Figure 4.1b displays three different TACs associated with different tissues: lungs (blue), heart (green) and liver (red). Here we have been using the d_1 distance. More information about this data set will be given in chapter 5.

After a particular template TAC is specified, we can compute the distance of the TACs at all other voxels to this template TAC which results in a scalar volume. This volume can now be rendered using classical (scalar) volume rendering algorithms. Our system currently can render a byte scalar volume at high frame rates. For example, Figure 4.2 shows the histogram and template TAC determined for a synthetic data set. Using standard transfer functions, we can now render the underlying data set.

4.3 TAC and Euclidean Distance Two-Dimensional Histogram

While discriminating simply on the TAC distance can be quite effective, we also wish to distinguish between body parts, that have similar TACs, but are separated from each other (e.g. the right and the left lung). In order to do so, we also include the Euclidean distance (d_E) and create a 2D histogram. Here, the x-axis provides the Euclidean distance and the y-axis the TAC distance (d_1, d_2 or s_C). Hence, we can specify colour and opacity using a 2D histogram (as pictured in Figure 4.3). The user simply draws a rectangular region over the data of interest. A color and opacity value can then be assigned to this region, which will be inherited by all data points included in this region.

As one can see in Figure 4.4, we are not able to separate right from left lung. This is due to the fact that the orthogonal separation of the Euclidean distance and TAC distance is not sufficient. Since both Euclidean and TAC distance are computed from the template TAC and corresponding voxel location, a carefully chosen template TAC is very crucial. Along the axis which provides the Euclidean distance, the 2D histogram only shows the distance to the location of template voxel. Voxels with the same Euclidean distance to the template voxel will lay on a sphere with the template voxel at its center, which is not intuitive and sufficient for users to assign a transfer function in order to highlight the areas of interest. Hence, we need an alternative way to visualize the data.

4.4 Layout by Multidimensional Scaling

In scalar volume rendering one often uses the histogram (or modified histograms, see [9, 53]) as an aid to determine features in the data set. This approach is not straightforward for TAC-based volumes. In order to use a histogram, both the carefully designed distance metric and template TAC are required. The process of choosing or designing an appropriate template TAC requires the knowledge about the dataset. Otherwise, the resulting histogram cannot be interpreted intuitively. Assuming no template TAC is available, we simply compute a distance from each TAC in the volume to all of the other TACs. This gives an nxn distance matrix (assuming n to be the number of voxels in the data set). This distance matrix is the input to a standard multi-dimensional scaling (MDS) algorithm that embeds the space of all TACs into 2D, such that the distance distortions are minimized. Given this 2D embedding we can now use it in order to specify a 2D colour and opacity transfer function. Here we use the same transfer function specification method as for the 2D histograms in Section 4.3. Figure 4.5 illustrates the transfer function assignment and corresponding volume rendering.

While we also could have chosen an embedding into 1D or 3D space, we felt that a 1D embedding would sacrifice the separability of the clusters too much and that the specification of a transfer function in 3D would be too difficult. Specifying the transfer function in 2D is still manageable and can be provided through an intuitive interface.

Again, in order to differentiate body parts that are separated in space, but have similar tracer behaviour, we assign a weighted TAC distance that balances Euclidean and TAC distances:

$$d(v_i, v_j) = (1 - \alpha)d_E(v_i, v_j) + \alpha d_p(v_i, v_j) \tag{4.9}$$

where $p \in 1, 2$ and $\alpha \in [0, 1]$. One drawback of the similarity measure s_C is that it cannot really be applied in such a setting, since there is no obvious calibration with the Euclidean distance. While the distance between two equal TACs will always be zero for d_1 and d_2, it can assume an arbitrary value for s_C.

Here we use α in order to weight between Euclidean distance and TAC distance. The TAC distance and Euclidean distance are normalized between zero and one. Figure 4.6 shows the influence of the Euclidean distance on the layout of a phantom data set by assigning different weights. The phantom data set models a myocardial perfusion SPECT study and the detail description of the data sets will be given in Chapter 5.

In order to assess the impact of this weighting, we colour coded the layout according to a pre-classified synthetic data set, as shown in Figure 4.6a. However, normally the assignment of colour and opacity happens after the initial 2D embedding using MDS, which is illustrated by Figure 4.5. Figure 4.7 shows the similar colour coded result to the layout of another phantom data set. The phantom data set is used to model different dynamic behaviour of activity in the oblique slice of the heart and corresponds to a series of $64 \times 64 \times 1$ slices spanning over 40 time frames.

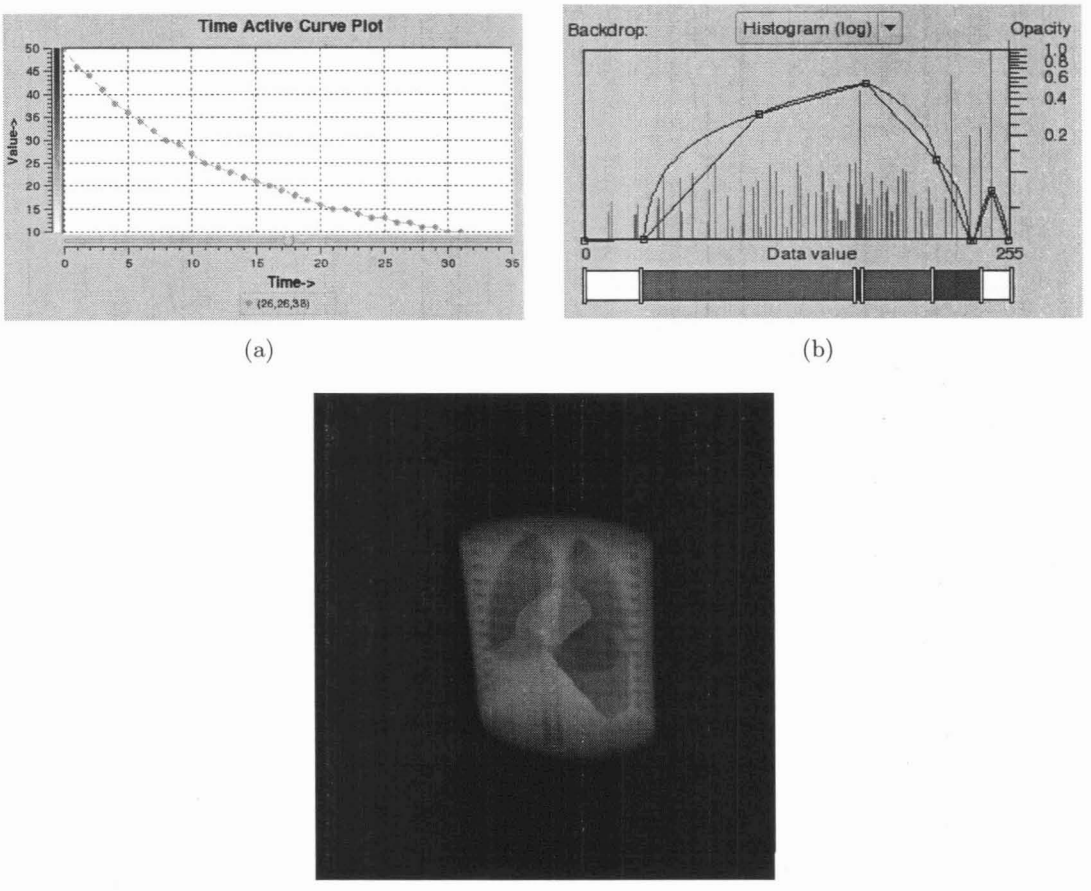

(a) (b)

(c)

Figure 4.2: Transfer function assignment and volume rendering of the distance volume to the template TAC. (a) The template TAC. The position of the corresponding voxel is shown at the bottom. (b) The histogram of the distance volume (using distance d_1) and an associated transfer function. (c) Volume rendering of the distance volume.

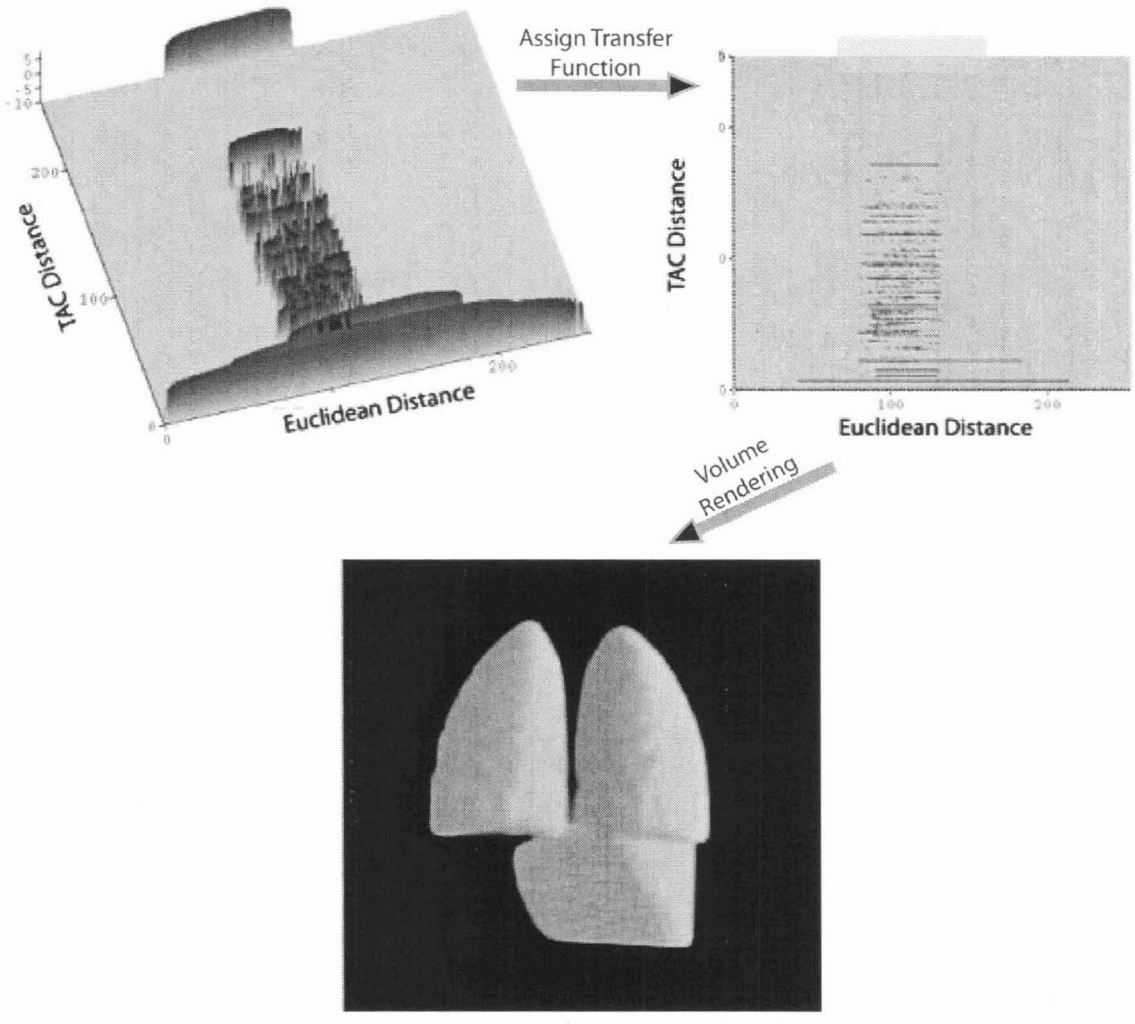

Figure 4.3: A Euclidean and TAC distance 2D histogram of the distance 3D volume. In the 2D histogram, one axis shows the TAC distance to the template TAC. Another axis shows the Euclidean distance to the corresponding voxel of the template TAC. A transfer function can be assigned directly to the 2D histogram in order to highlight the region of interest.

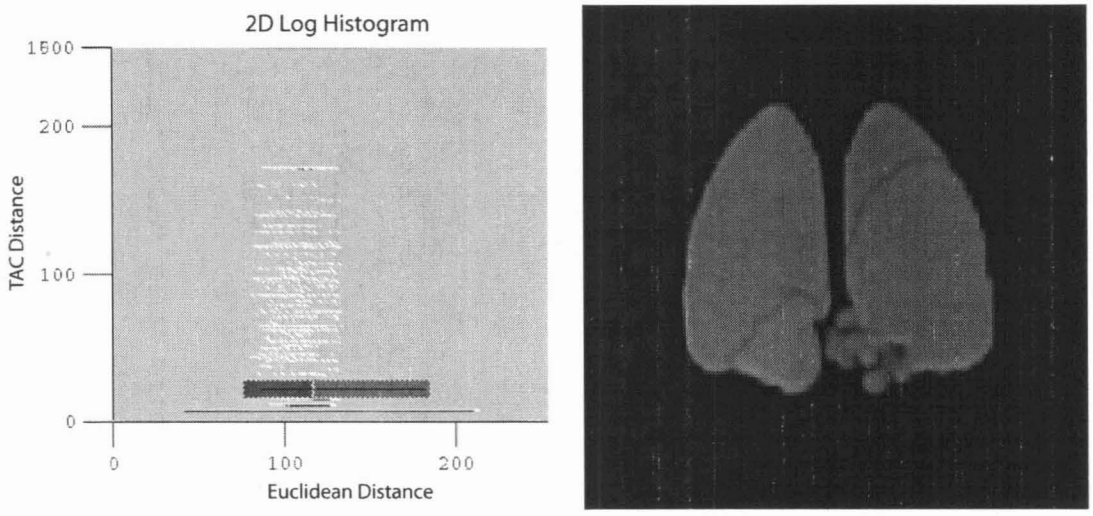

Figure 4.4: Transfer function assignment (left) on TAC and Euclidean distance 2D histogram will not be able to segment the left and right lungs (right).

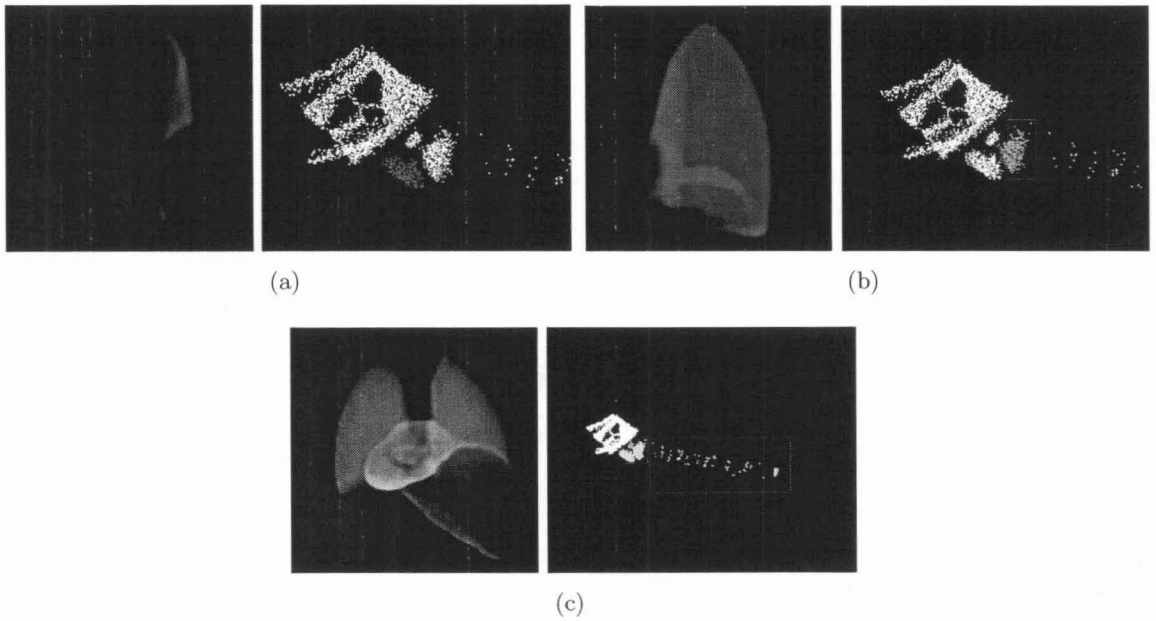

Figure 4.5: The MDS layout using a similarity distance of $67\%d_1 + 33\%d_E$ and a transfer function assignment on the right with the corresponding volume rendering on the left. (a) the left lung segmentation (b) the right lung segmentation (c) a complete segmentation of the dynamic MCAT data set.

(a)

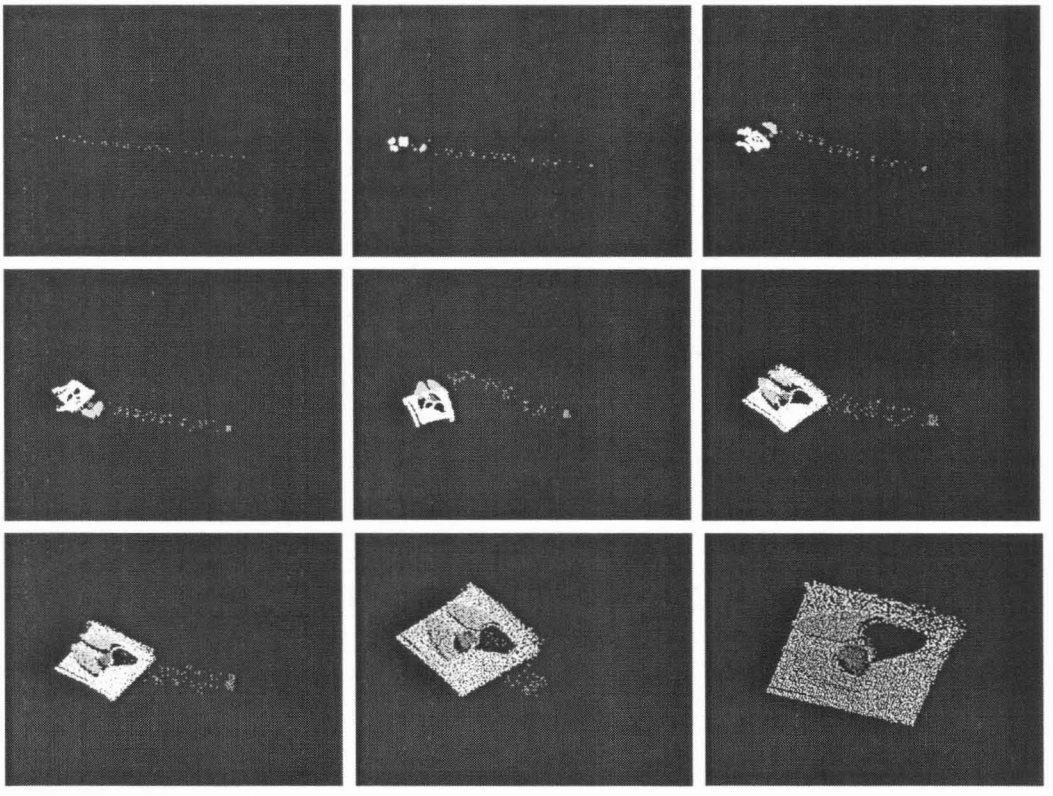

(b)

Figure 4.6: (a) The phantom data set used for modelling a myocardial perfusion SPECT study. (b) The result of the MDS layout using different weights (from left to right): (top row) $1d_1+0d_E, 0.9d_1+0.1d_E, 0.8d_1+0.2d_E$; (middle row) $0.7d_1+0.3d_E, 0.6d_1+0.4d_E, 0.5d_1+0.5d_E$; (bottom row) $0.4d_1 + 0.6d_E, 0.3d_1 + 0.7d_E, 0.2d_1 + 0.8d_E$;

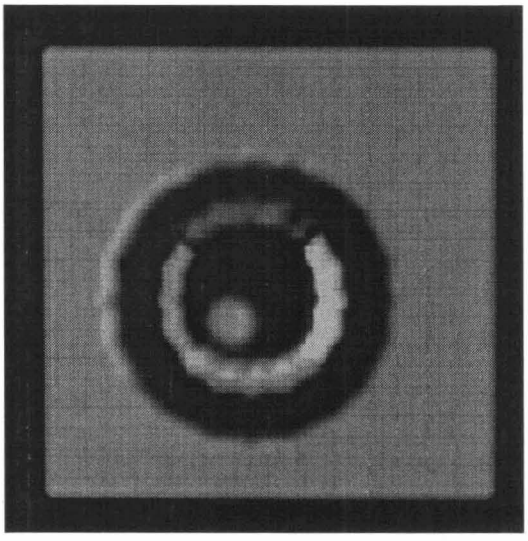

(a)

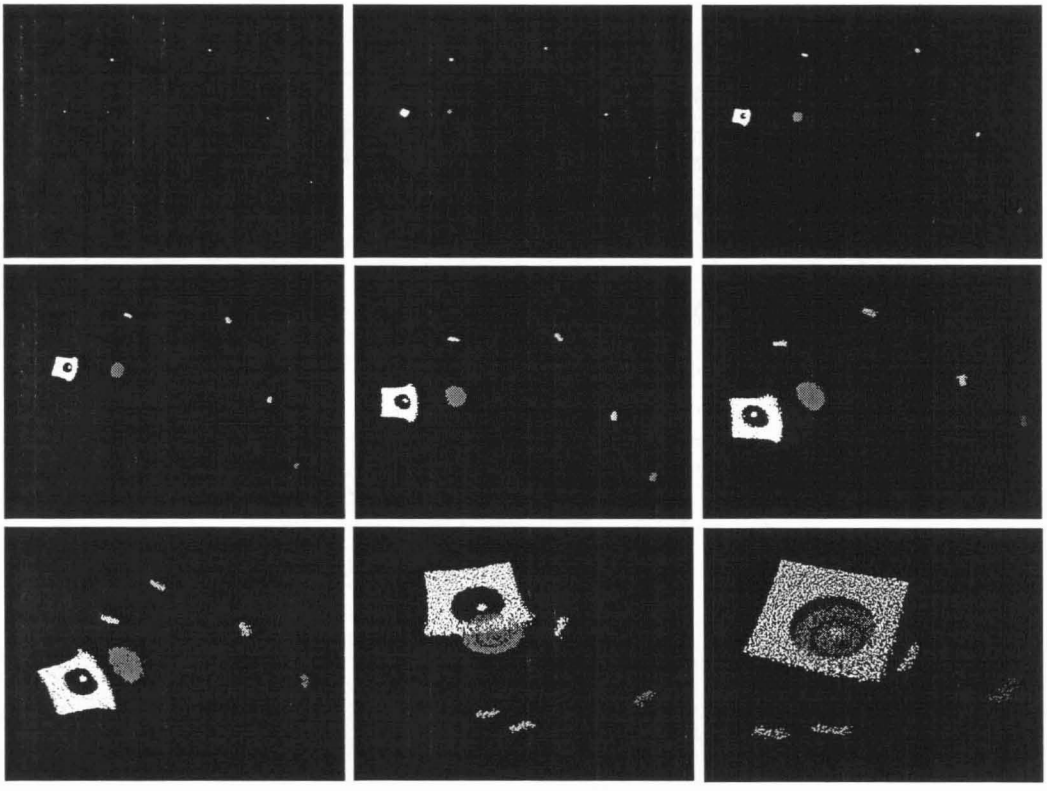

(b)

Figure 4.7: (a) Another phantom data set used to model different dynamic behaviour of activity in the oblique slice of the heart. (b) The result of the MDS layout using different weights (from left to right): (top row) $1d_1 + 0d_E, 0.9d_1 + 0.1d_E, 0.8d_1 + 0.2d_E$; (middle row) $0.7d_1 + 0.3d_E, 0.6d_1 + 0.4d_E, 0.5d_1 + 0.5d_E$; (bottom row) $0.4d_1 + 0.6d_E, 0.3d_1 + 0.7d_E, 0.2d_1 + 0.8d_E$;

Chapter 5

Results

5.1 System environment

In order to implement our ideas we use the vuVolume framework [1]. This framework has been developed in our Graphics, Usability and Visualization lab (GrUVi), Simon Fraser University, and is available on sourceforge for download. Since vuVolume focuses on volume rendering of scalar data, we extended its capabilities to deal with time-varying data.

The basic environment can be seen in Figure 5.1. First we load the data using the widget (1). Then the user determines a template TAC by specifying its (x, y, z) location (see (2)). A yellow marker appears in the volume in order to guide the user's selection (see the render window (3)). Further, the TAC will be displayed in the TAC widget (4). Next, the user can pick one of the three distance metrics ($d_1.d_2$, or s_C) (see (5)). After the distance volume is computed, the histogram is being displayed in the histogram widget (6). Now the user can interact with the scalar volume, like in any traditional volume rendering environment. Instead of using the traditional 1D histogram-based transfer functions, the user can switch to a 2D histogram, spanned by the Euclidean distance and the chosen TAC distances by picking the proper tab at (7). The alternate GUI elements have been explained in Figure 4.3 and the screen capture is displayed in Figure 5.2.

Alternatively, when no template TAC is chosen, the user still has to pick a similarity measure before being able to switch to the MDS view using the widget (7). The screen capture is displayed in Figure 5.3.

[1] http://sourceforge.net/projects/vuvolume/

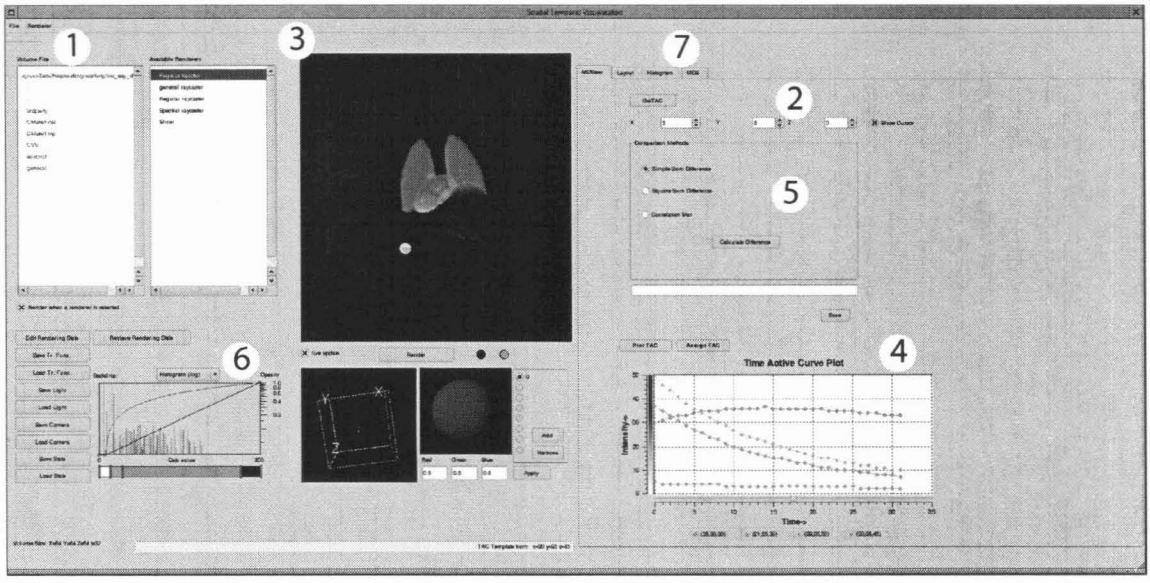

Figure 5.1: Screen-capture of the 3D+time visualization and exploration application. The GUI includes panes for volume rendering, viewing TACs, 1D histograms and specifying a 1D transfer function, 2D histograms and a 2D transfer function, MDS, choice of TAC dissimilarity metric and more. The left half part is volume rendering and the right half is where the user can choose one of the different methods in order to analyze the data sets.

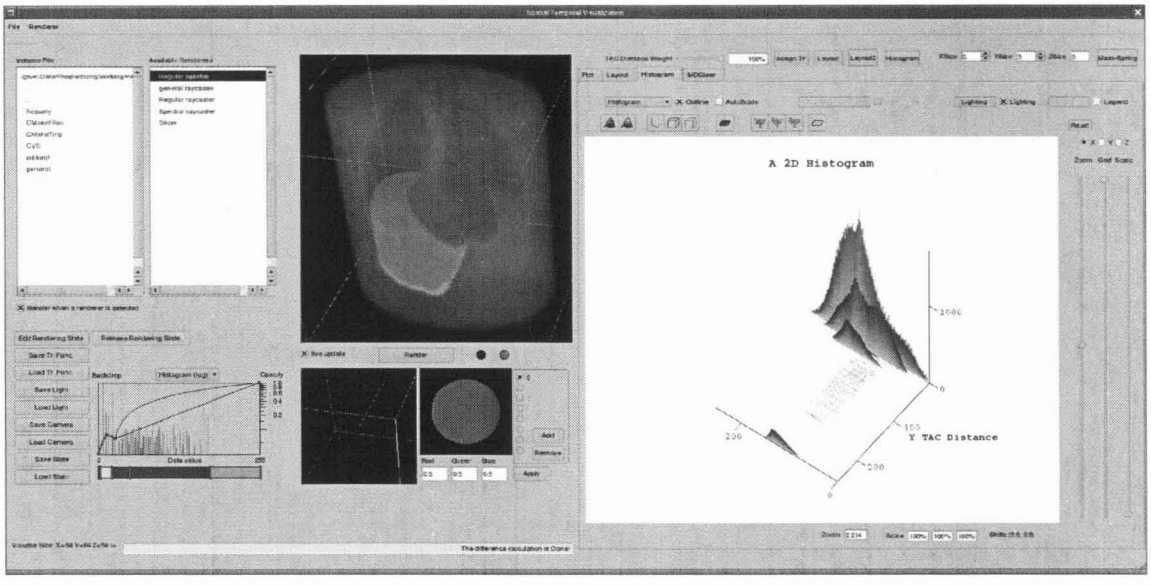

Figure 5.2: Screen-capture of the 3D+time visualization and exploration application. The left half part is volume rendering and the right half displays the 2D histograms where the user can assign a 2D transfer function directly.

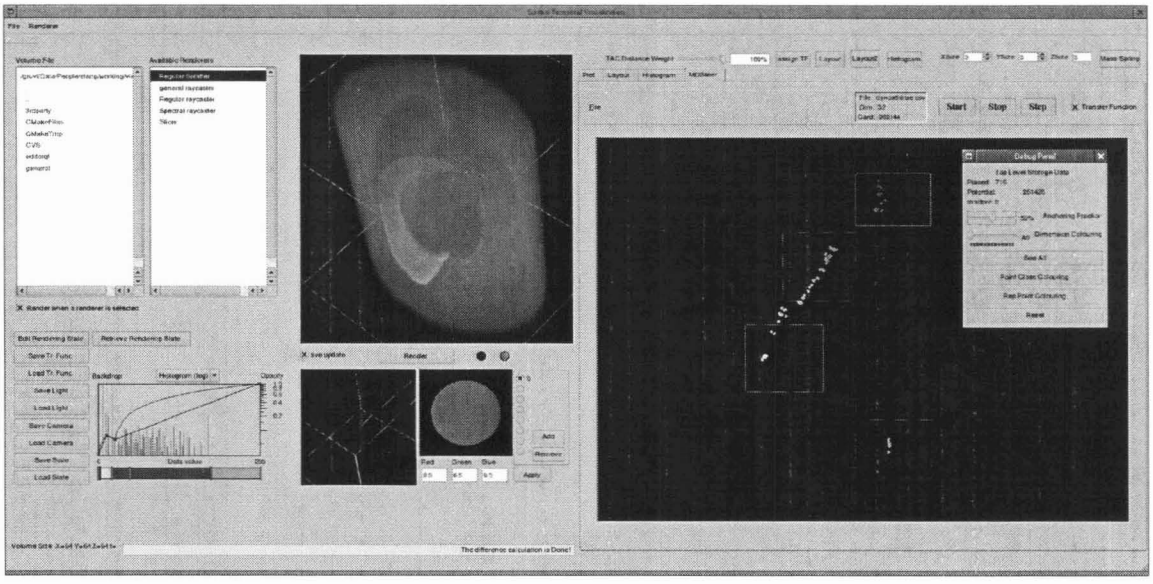

Figure 5.3: Screen-capture of the 3D+time visualization and exploration application. The left half part is volume rendering and the right half displays the MDS layout where the user can assign a 2D transfer function directly.

5.2 Assessment of the different TAC metrics

In the following experiment we assess the strengths and weaknesses of different TAC similarity measures with noise interference. In order to do so, we generate a template TAC $v(t)$ with log-normal distribution. (See Figure 5.4(a).) We add uniform noise $n(t)$ to this synthetic template TAC $v(t)$ in order to judge the robustness of the similarity measure. Hence, we are producing a signal

$$v_n(t) = v(t) + \alpha/100 * n(t) \tag{5.1}$$

where we are assuming that $n(t) \in [-1, 1]$. In Figure 5.4(b), we plot the similarity measure $d(v(t), v_n(t))$ as α is changing between 0 and 100 (where d stands for d_1, d_2, or s_C). While both, d_1 and d_2 will start at point $(0, 0)$, the maximum correlation s_C naturally is not zero. Since we don't care about the particular value of the maximum correlation of $v(t)$, we normalize this curve by $s_C(v(0), v_n(0))$. Further, to make the trend more clear, we do a least-squares fit of all three curves, and compute their slopes. The result of this test is displayed in Figure 5.4(c). As uniform noise increases, d_1 increases fastest and s_C increases the least among the three methods. It clearly shows that d_1 is most sensitive and s_C is least

sensitive to uniform noise.

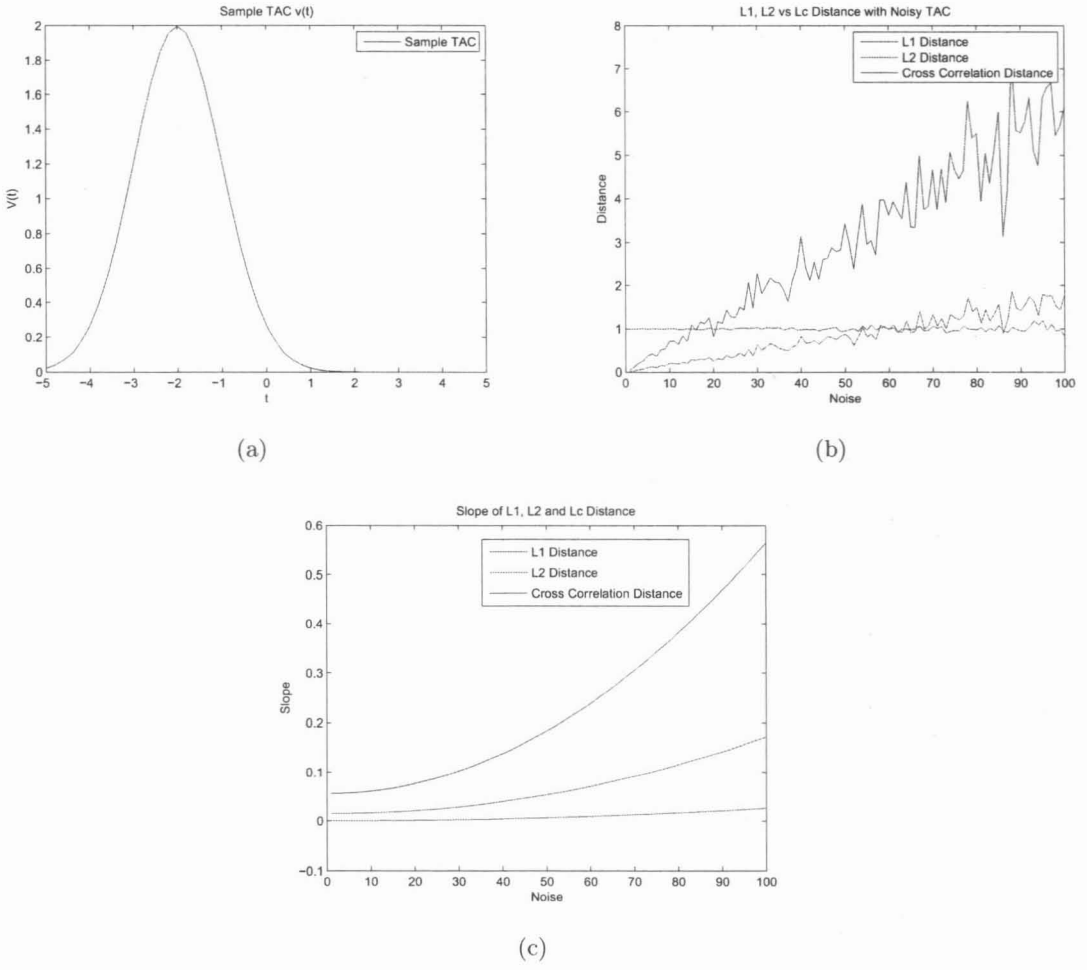

Figure 5.4: (a) Template TAC (b) d_1, d_2 and s_C distance between noise TACs and template TAC. (c) The slope of d_1, d_2 and s_C distance between noise TACs and the template TAC.

Under noise interference, the measure s_C is clearly preferable over d_1 and d_2. Further, d_1 is more sensitive to uniform noise compared to d_2. However, s_C and d_2 may also smooth out some important features, but d_1 will be able to keep these features. Therefore, d_1 will be preferable for non-noise and some low-noise datasets.

5.3 Phantom and patient data

Our visualizations and studies presented in the earlier images of this paper are all based on a dynamic version of the MCAT phantom [70]. The adaptation of the static MCAT phantom to a dynamic setting was done by the Medical Imaging Research Group (MIRG) at the Vancouver General Hospital. The spatial data set corresponds to a series of $64 \times 64 \times 64$ matrices spanning 32 time frames. This phantom models a myocardial perfusion SPECT study. It reproduces a distribution of the dynamic radiotracer teboroxime in the heart and all other organs of the thorax.

The challenge in SPECT heart studies is to differentiate photons that originate from liver from these originating from the heart, as scattered liver photons often appear as if they are emitted from the heart and may hide myocardial perfusion defects. Since the dynamic behaviours of the tracer in the liver and in the heart are different, their respective TACs can be used to differentiate between the two groups of photons and to correctly segment and visualize the two organs. Figure 5.5 shows the best separation of liver and heart for the three similarity measures d_1, d_2, and s_C. The corresponding distance volume histogram and transfer function are also shown with rendered images. The initial template TAC was chosen to be a simple flat zero TAC created from a voxel outside any region of interest. While this resulted in an easy distinction between heart and liver for the d_1 and d_2 distances, such a template TAC is not usable for the s_C distance. Since the correlation of any TAC to a zero TAC will result in a "zero" value, we have to select another template TAC. Hence, we used a TAC from the heart region. After a considerable amount of data exploration, the best separation that we could achieve was found and is presented in Figure 5.5c.

	Number of Voxels		
Methods	Heart	Liver	Lung
original	1947 (voxels)	7148 (voxels)	17544 (voxels)
d_1 distance	100%	100%	100%
d_2 distance	100%	100%	100%
s_C distance	96.8%	100%	98.8%

Table 5.1: Comparing the performance of segmentation of the dynamic MCAT data with different similarity measures. The table depicts the percentage of correctly labeled voxels.

Since this is a synthetic data set we know exactly which voxels are part of the liver tissue and which are part of the heart tissue. Table 5.1 presents the accuracy of our segmentation

using our three different similarity measures. Since this is a noise free synthetic data set, we can see that the d_1 and d_2 similarity measures perform best and the noise robustness of the s_C is not being exploited.

The second type of data we have worked with was a simulation of a dynamic PET brain study. It was created using PET-SORTEO [56]. The data set that we used has $128 \times 128 \times 63$ spatial voxels and 27 time frames. In clinical practice the striatum and cerebellum are typically regions of interest which one would want to analyze and visualize [36]. Hence, we select a template TAC corresponding to a voxel which belongs to this part of the brain. (See the yellow glyph in Figure 5.6f.) We calculate the d_1 distance between the template TAC and all other TACs; the resulting volume is visualized by volume rendering. (See Figure 5.6e.) The striatum shows a different d_1 distance and is highlighted (green) inside the brain (red) in Figure 5.6e. A TAC (green) from the striatum is extracted and displayed in Figure 5.6e in order to compare it with a TAC (red) from the brain. Figure 5.6a and b show the MDS layout of TACs with a combined similarity measure of $100\%d_1$ and $50\%d_1 + 50\%d_E$ respectively. The points are color coded to match the color of the volume rendering. The points in green are associated with TACs in the striatum area; points in red are associated with TACs in the brain area; points in yellow are associated with TACs in the skin, while background TACs are white.

The third type of data we have worked with was a dynamic series of planar images corresponding to a renal patient study. The planar image has $128 \times 128 \times 1$ spatial voxels and 102 time frames. Physicians use these dynamic planar images to evaluate the kidney function. In this case a zero template TAC was used. We first calculate the d_1 distance between the template TAC and all other TACs, which is then displayed in the histogram at the bottom of Figure 5.7a. We display the resulting 2D image in Figure 5.7c. This image was created with a transfer function presented at the bottom of Figure 5.7a. Figure 5.7b shows the MDS layout of TACs by using a similarity distance proportional to $1d_1 + 0d_E$. Figure 5.7c clearly shows that one of this patient's kidneys (red) is healthy as it has a normal TAC. The other kidney (green) displays abnormal temporal behaviour (as can be seen in Figure 5.7a and b) which is related to the fact that its function is altered by some disease. The green halo around the red kidney shows that this part has low active temporal behaviour. This example shows how our method can potentially help in clinical diagnosis by identifying organs or areas which are characterized by TACs different from that of a normal tissue.

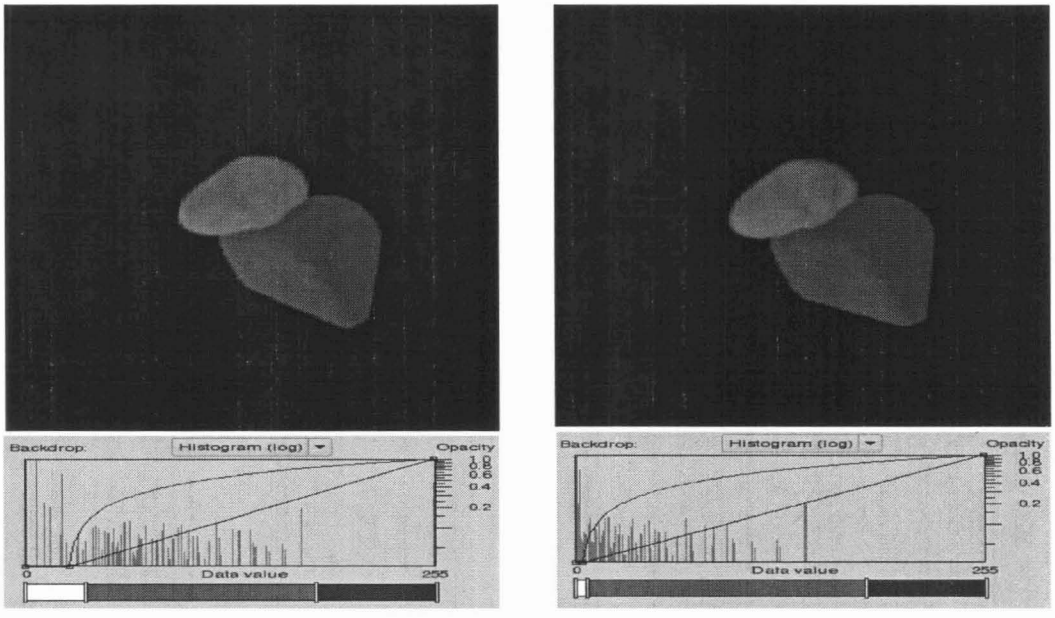

(a) (b)

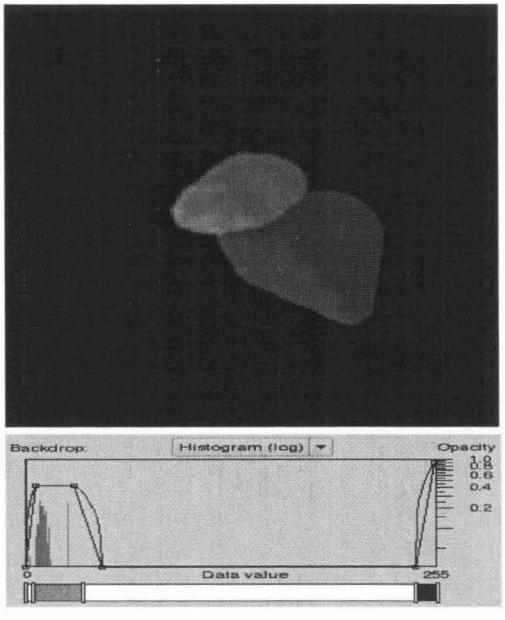

(c)

Figure 5.5: Volume rendering, histogram and transfer function for the dynamic MCAT phantom using different similarity measures and template TACs. (a) d_1 distance and a zero TAC as template. (b) d_2 distance and a zero TAC as template. (c) s_C distance and a heart TAC as template.

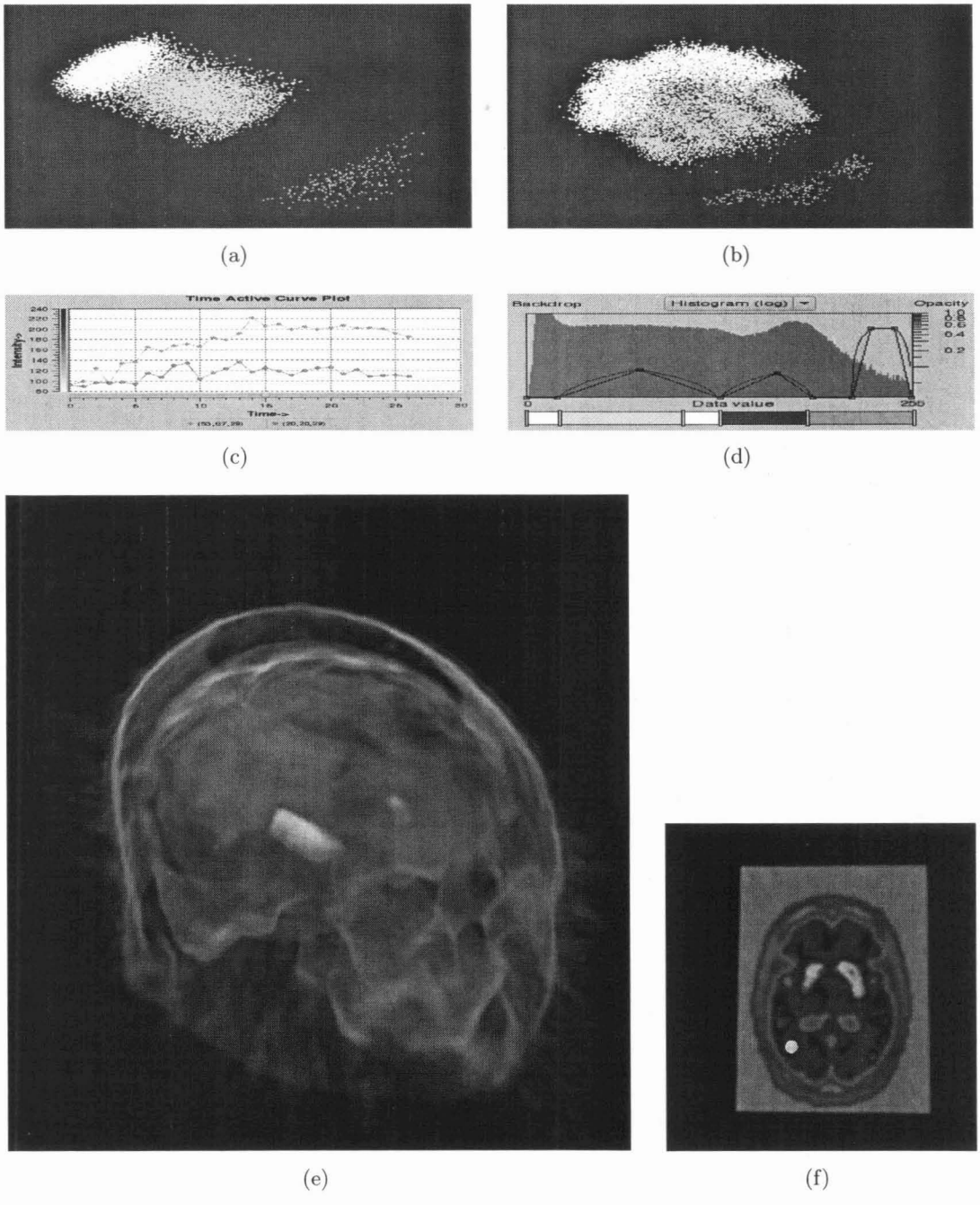

Figure 5.6: Simulated dynamic PET data set (based on PET-SORTEO): (a) The MDS layout using a similarity distance proportional to $100\%d_1$ (b) The MDS layout using a similarity distance proportional to $50\%d_1 + 50\%d_E$. (c) The TAC of a voxel in the striatum area (green) and the template TAC in the brain area (red). (d) The transfer function used to render the image in (e). (e) Volume Rendering based on the transfer function in (d) using a template TAC in the brain and the d_1 distance. (f) The position (yellow dot) of the template TAC.

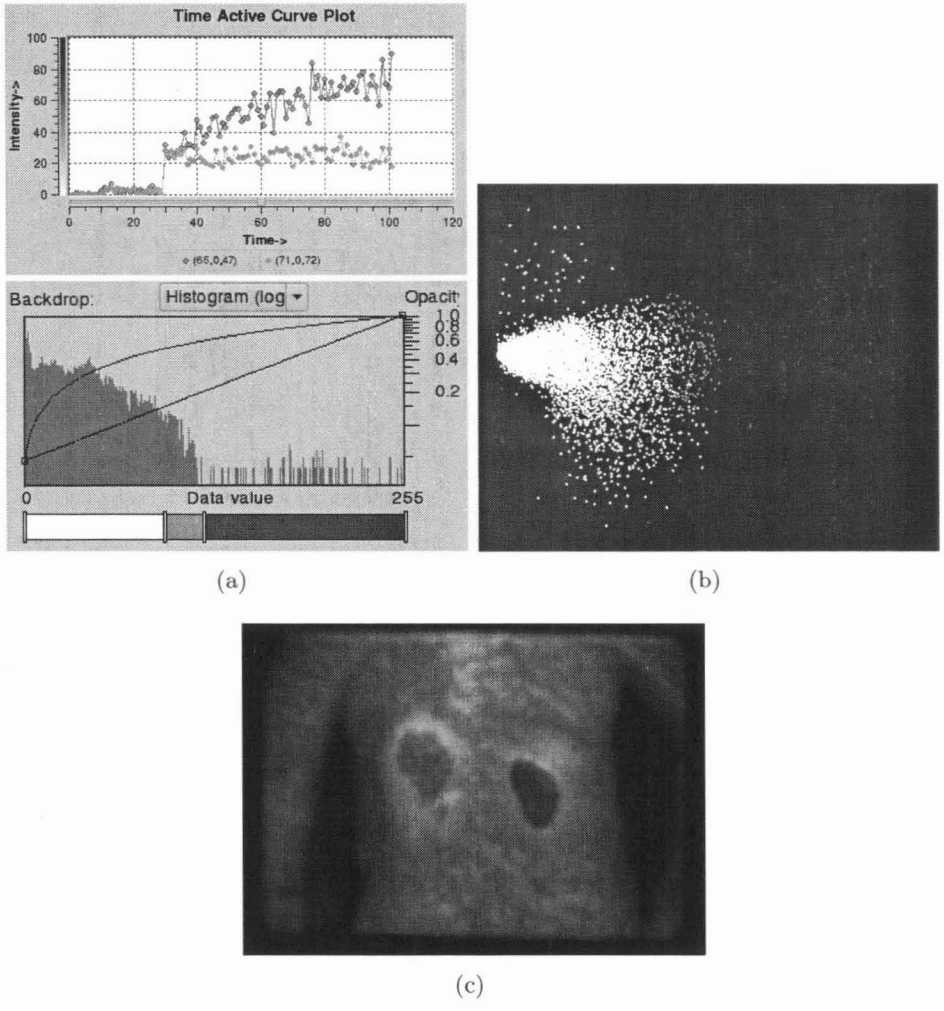

(a) (b)

(c)

Figure 5.7: Data set of a dynamic nuclear medicine (single photon) study: (a-top) The TAC of a voxel in the healthy kidney area (red) and the abnormal area (green). (a-bottom) The transfer function used to render the image in (c). (b) The MDS layout using a similarity distance proportional to $1d_1 + 0d_E$. (c) Display of the slice (not rendered) with the colour assignment set in part (a-bottom).

Chapter 6

DTMRI Visualization

Diffusion tensor magnetic resonance imaging (DTMRI) has become an important tool to measure biological tissues at the microscopic level. It has attracted attention in the field of medical image processing and visualization. Because each voxel in a three-dimensional diffusion tensor MRI scan is a symmetric and positive semi-definite 3×3 matrix, the data cannot be segmented and interpreted simply by inspecting grayscale images of scans. It is also a challenge to visualize the many interrelated components between tensors by traditional methods.

This chapter will start with an introduction to DTMRI and its underlying meaning. Then, previous work on diffusion tensor imaging (DTI) visualization methods will be given. An affine invariant tensor dissimilarity measurement will be discussed. A new DTI visualization method will be examined at the end of the chapter.

6.1 Introduction

The term "tensor" was originally introduced to describe tension forces in solid bodies with an array of three-dimensional vectors from physics and engineering. In the field of diffusion tensor magnetic resonance imaging (DTMRI), a tensor quantity that expresses the differential permeability of organs to water in varying directions is used to produce scans of the brain.

In 1827, the botanist Robert Brown observed the movement of pollen particles floating in water under the microscope. Later, the phenomenon of water diffusion became known as Brownian motion. Thorvald N. Thiele was the first person to describe the mathematics

behind Brownian motion. Albert Einstein conducted research on the problem and drew the attention of physicists.

Diffusion is the transport of one material through another by the random microscopic motion of molecules. Molecular motion is affected by the properties of the medium in which it occurs. Molecular motion or diffusion within biological tissues reflects both tissue structure and architecture at the microscopic level. There are two types of diffusion:

- Isotropic diffusion, and
- Anisotropic diffusion.

In pure water, the medium does not restrict molecular motion and diffusion is the same in all directions. This is an isotropic diffusion. However, the coherent organization of axons, for example, in white matter permits water to diffuse faster along the axon path than across it. The molecular motion in white matter is anisotropic. DTMRI is an indirect indicator of the microscopic physical organization of tissue.

Diffusion weighted imaging (DWI) is a modification of regular MRI techniques. It produces magnetic resonance images of biological tissues weighted by water diffusion. In DWI, MRI produces contrast images of either water molecules in a sample excited by the imposition of a strong magnetic field ($T1$-weighted images) or measuring the loss of coherence or synchrony between the water protons ($T2$-weighted images) [29]. DWI only measures the local characteristics of water diffusion and can produce images directly from scanning. However, DTI data requires post-processing, since several MRI scans of image data including a $T2$-weighted image and at least six DWI data, are required to calculate 6 independent parameters for each 3×3 tensor matrix. With the introduction of DTI, anisotropic diffusion effects in diffusion MRI data could be fully characterized and exploited.

In order to provide an initial feel for what diffusion tensor data looks like, Figure 6.1 shows one midsagittal slice through a DTMRI scan. It is visualized with a matrix of images each of which displays a single component of the matrix representation of the diffusion tensor. With this type of visualization, the tensor information is visualized by a scalar and the overall three-dimensional structure is not shown.

Our methods first apply the distance measurement methods proposed by Vemuri et. al. [73] between a template tensor and every other tensor. This reduces the tensor to a scalar, which represents the similarity of anisotropic diffusion orientation between tensors and the template. We then visualize the resulting scalar volume by direct volume rendering.

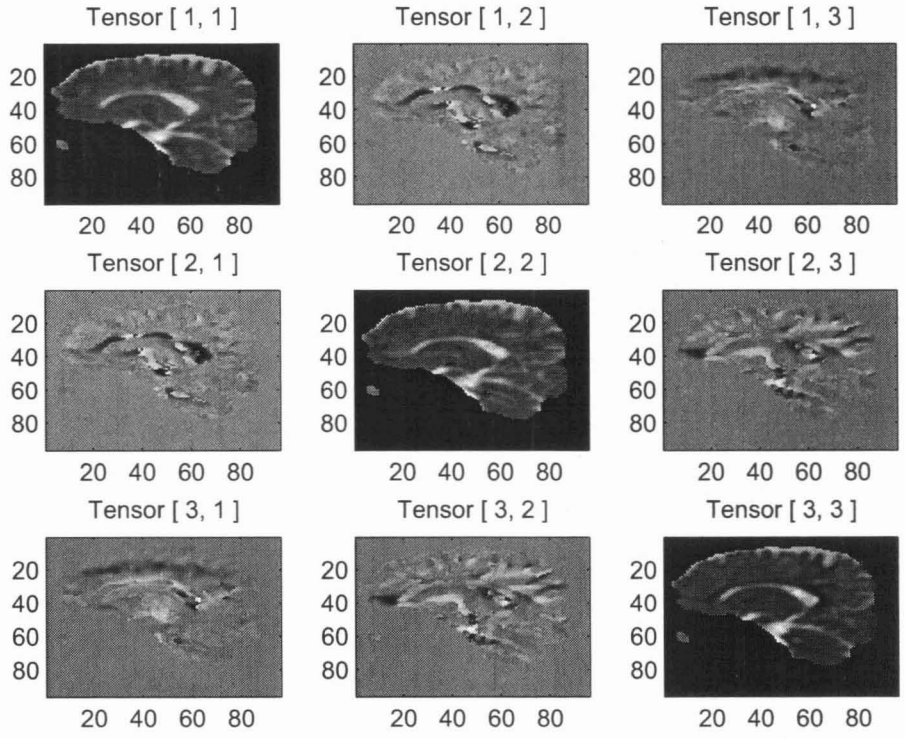

(a)

Figure 6.1: Visualization of diffusion tensor components

The remainder of this chapter starts with a review of different diffusion tensor image analysis and visualization methods. The data format will also be given in the following section. Several scalar indices for diffusion tensors will be discussed. The chapter ends with our proposed DTI visualization method.

6.2 Diffusion Tensor Imaging Analysis and Visualization

During the image acquisition stage, the data from the MR scanner is noisy and contains various artifacts. The noise and artifacts will cause errors when reconstructing the DTI. For example, errors can cause the constructed fibres to point in the wrong direction and thus lead to a wrong visualization. Many techniques have been applied to denoise the medical images in the scalar fields. Recently, several methods have been proposed to reduce noise

in DTI, such as median filtering and morphological operations [43, 14].

There is much work on scalar and vector image segmentation achieved by applying a geometric active contour model [45, 68, 16]. Zhukov et al. [87], propose a pipeline to segment DT-MRI datasets. The pipeline starts with the computation of an invariant anisotropy measure from raw diffusion tensor data. The geometric models of the brain structures are then constructed. The level set method is also applied to remove noise from the data and to produce a smooth, geometric model. Feddern et al. [23] extend several level set methods to tensor-valued data.

In tensor image segmentation, one important issue is to define the proper tensor distance that measures the similarity and dissimilarity between tensors. Any kind of matrix norm could generally be used to measure the tensor distance. One simple way is to apply a tensor Euclidean distance in tensor field restoration [19, 74]. Alexander et al. [5] discuss and compare a number of similarity measures applied to the task of registration of 3D images of the human brain. Tsuda et. al. [69] introduce the information geometry of positive definite matrices and then use it in an "EM" algorithm to approximate an incomplete kernel. Recently, Wang and Vemuri [73] proposed an affine invariant tensor dissimilarity measure method. The affine invariant is an important property for the DTI segmentation. We will adopt the distance measurement method for our visualization.

In order to segment and visualize DTMRI, the tensor field must spatially be aligned with other imaging modalities, such as $T1$- and $T2$-weighted MRI. To allow the comparisons between individuals, algorithms for establishing pointwise correspondences between DTMRI are required. Image registration is used to establish the pointwise correspondence. Several DTMRI registration algorithms [4, 58] have been proposed recently.

The visualization of DTI is a challenge. Currently, there is no well established method to display the matrix values which tensor data represents. Meaningful DTI visualization methods depend on the specific application domain. Also, the trade off between complexity and legibility should also be considered when one designs a visualization method.

The widely accepted tensors to describe diffusion can be visualized as ellipsoids. It is a natural choice of glyph to visualize DTI data [15]. The directions of the main axes represent the eigenvectors and their lengths the eigenvalues of the tensor. The longest main axis denotes the value and direction of maximum diffusion, whereas the shortest axis represents the value and direction of minimum diffusion. Since the diffusion process is much faster along the direction of the fibers in white matter, the longest main axis of the diffusion ellipsoid

denotes the direction of the fibers and is much larger than the other two in white matter [60]. If the diffusion is isotropic, the diffusion tensor can be visualized as a sphere. Laidlaw et al. [37] proposed two approaches to visualize DTI. The first approach could display ellipsoids simultaneously in context by normalizing them to approximately the same size. Laidlaw et al. also applied a concept from oil painting to represent the tensor data with multiple layers of varying brush strokes in the second proposed DTI visualization approach. Westin et al. [77] combined and color coded linear, planar and spherical components with the ellipsoids to visualize the tensor data. Kindlmann [33] presented a new tunable continuum of glyphs based on superquadric surfaces to avoid asymmetry and visual ambiguity by using an ellipsoidal glyph.

However, it is hard to represent continuous diffusion phenomena by discrete glyphs. Tractography, a term first used by Basser et al. [11], was proposed to address this problem. The basic idea is to use streamlines instead of glyphs to represent the tensor data. Xue et al. [82] present a fiber path by a curve after fiber projection reconstruction. Zhang et al. [84] used streamtubes and streamsurfaces to visualize DTI. One problem of tractography is its sensitivity to noise. Some work [12, 75, 86] has been done to address this problem.

Direct volume rendering is widely used to visualize scalar data. Transfer functions are applied to map the scalar value to optical properties, such as colour and opacity. Kindlmann et al. [32] extend volume rendering to visualize DTI by applying various types of diffusion tensor transfer functions. Zhang et al. [85] gave a thorough survey of different tensor visualization methods.

6.3 Data and Data Format

We use two DTI data sets to test our new visualization methods. One is the DTI data of a brain scan and the other is the DTI data of a cardiac scan. The eigenvalues and corresponding eigenvectors are stored in two separate files for each of the data sets. The file is in the Matlab data file format with the file extension *.mat*. The eigenvalues for the DTI brain data set are stored in a $96 \times 96 \times 3 \times 66$ four-dimensional matrix and the corresponding eigenvectors are stored in a $96 \times 96 \times 3 \times 3 \times 66$ matrix. Similarly, the eigenvalues for the DTI cardiac data are stored in a $21 \times 32 \times 3 \times 21$ four-dimensional matrix and the corresponding eigenvectors are stored in a $21 \times 32 \times 3 \times 3 \times 21$ matrix. Here, we should point out that most of the work presented in this thesis uses the DTI data of the brain scan.

In order to load the data sets into our system, the matlab data have to be converted to a NLM Insight Toolkit (ITK) [28] readable format. In our application, we chose to convert to the MetaImage data format. MetaImage is a simple but powerful text-based tagged file format for medical images. A MetaImage file contains a text header to describe the meta information of the data and binary data to store the actual data. MetaImage header files usually require either ".mha" or ".mhd" extensions. If the data is stored in multiple files, the header file should indicate where to find these files. The following is a simple example of a MetaImage header file.

NDims = 3
DimSize = 512 512 100
ElementType = MET_USHORT
ElementSize = 1 1 3
ElementSpacing = 1 1 1
ElementByteOrderMSB = False
ElementDataFile = LIST
filenameOfDataFile1
filenameOfDataFile2
filenameOfDataFile3
filenameOfDataFile4
...

- *NDims* indicates the dimensionality of the data. The example above is a 3D data set.
- *DimSize* describes the size of the volume in terms of voxels along each direction.
- *ElementType* indicates the primitive type used for each voxel. For the above example, the "unsigned short" data type is used.
- *ElementSize* describes the physical size of each voxel along each direction.
- *ElementSpacing* indicates the distance between the neighbouring voxels along each direction.
- *ElementByteOrderMSB* describes whether the data is encoded in little or big endian order.

- *ElementDataFile* indicates whether the data is stored in several files or not. In the example above, "LIST" means the data is stored in several files. The name of each data file is listed after this line.

6.4 Scalar Metrics of Diffusion Tensors

Several scalar indices have been introduced to describe the diffusion tensor field. Rotational invariance or affine invariance are desirable properties for a scalar distance metric of a tensor. These properties allow the measurement between tensors to be independent on the coordinate system. Otherwise, knowledge of the coordinate system must be combined with the metric in order to give a proper interpretation. The diffusion tensor D is a 3×3 symmetric positive semi-definite matrix:

$$D = \begin{pmatrix} D_{xx} & D_{xy} & D_{xz} \\ D_{yx} & D_{yy} & D_{yz} \\ D_{zx} & D_{zy} & D_{zz} \end{pmatrix} \tag{6.1}$$

Several indices commonly used are the trace of the diffusion tensor, apparent diffusion coefficient, fractional anisotropy and relative anisotropy, all of which are rotationally invariant. The trace of the diffusion tensor D

$$T_r(D) = D_{xx} + D_{yy} + D_{zz} \tag{6.2}$$

measures the mean diffusivity of D.

The Apparent Diffusion Coefficient of a diffusion tensor D is simply the average of its diagonal elements

$$ADC = \frac{T_r(D)}{3} \tag{6.3}$$

Basser et. al. [10] proposed rotationally invariant anisotropy metrics: fractional anisotropy and relative anisotropy. Fractional anisotropy is defined as

$$FA = \sqrt{\frac{3}{2}} \frac{\sqrt{(\lambda_1 - < \lambda >)^2} + \sqrt{(\lambda_2 - < \lambda >)^2} + \sqrt{(\lambda_3 - < \lambda >)^2}}{\sqrt{\lambda_1^2 + \lambda_2^2 + \lambda_3^2}} \tag{6.4}$$

which is a measure of the magnitude of the tensor that can be ascribed to the anisotropic diffusion, where λ_1, λ_2 and λ_3 are the eigenvalues of the diffusion tensor D and

$$< \lambda >= \frac{\lambda_1 + \lambda_2 + \lambda_3}{3}. \tag{6.5}$$

Relative anisotropy is defined as

$$RA = \frac{\sqrt{(\lambda_1 - < \lambda >)^2 + (\lambda_2 - < \lambda >)^2 + (\lambda_3 - < \lambda >)^2}}{\sqrt{3} < \lambda >} \tag{6.6}$$

which is a normalized standard deviation representing the ratio of the anisotropic part of the tensor to its isotropic part.

Figure 6.2 shows the Apparent Diffusion Coefficient, Fractional Anisotropy and Relative Anisotropy of a sliced brain DTI dataset.

6.5 Tensor Distance and Visualization

To measure the distance between two tensors, Vemuri et. al. [73] proposed an affine invariant way to measure the "distance". In [69], Tsuda et. al. introduced the information theoretic "distance" measure by Kullback-Leibler (KL) divergence between two probability density functions p and q.

$$KL(p||q) = \int p(x) \log \frac{p(x)}{q(x)} dx \tag{6.7}$$

where $p(x)$ and $q(x)$ are the probability density functions. In order to symmetrize the KL divergence, a J-divergence is calculated as

$$J(p, q) = \frac{1}{2}(KL(p||q) + KL(q||p)) \tag{6.8}$$

Vemuri et. al. proposed a tensor distance for the symmetric positive definite tensors as the square root of the J-divergence in [73]

$$d(T_1, T_2) = \sqrt{J(p(r|t, T_1), p(r|t, T_2))} \tag{6.9}$$

where $p(r|t, D)$ is defined as

$$p(r|t, D) = \frac{1}{\sqrt{(2\pi)^n |2tD|}} e^{\frac{-r^T D^{-1} r}{4t}} \tag{6.10}$$

where tensor D has displacement r of water molecules at each lattice in the image at time t and n is the dimension of the tensor.

The equation 6.9 can be simplified as

$$d(T_1, T_2) = \frac{1}{2}\sqrt{tr(T_1^{-1}T_2 + T_2^{-1}T_1) - 2n} \tag{6.11}$$

where $tr(\cdot)$ is the matrix trace operator, n is the size of the tensor T_1 and T_2. $d(T_1, T_2)$ has the affine invariant property, which is given in [73]. We choose the tensor at $(40, 60, 33)$, a tensor located in the corpus callosum, as a template and calculate the distance between the template tensor and every other tensor. Direct volume rendering is then applied to the distance volume. To get a feeling of the Vemuri distance in the brain volume dataset, Figure 6.3(a) shows the distance by using volume rendering. Figure 6.3(b) shows the corresponding histogram of the volume and the transfer function to generate image (a). During the transfer function assignment process, a user can choose either the logarithmic or regular histogram from a drop-down menu to be shown at the background of the widget in Figure 6.3(b). Based on the choosen histogram, a user can specify the opacity value, which is defined by the curve on top of the histogram, and the RGB value, which is defined at the bottom of the widget in Figure 6.3(b). The corpus callosum and medulla, both of which have similar fibres, are clearly highlighted by a red color in Figure 6.3(a). The corresponding transfer function clearly shows that tensors in both corpus callosum and medulla have relatively large but small range of distance to the template tensor. The small distance range also indicates that fibres in the corpus callosum and medulla have a very similar diffusion orientation.

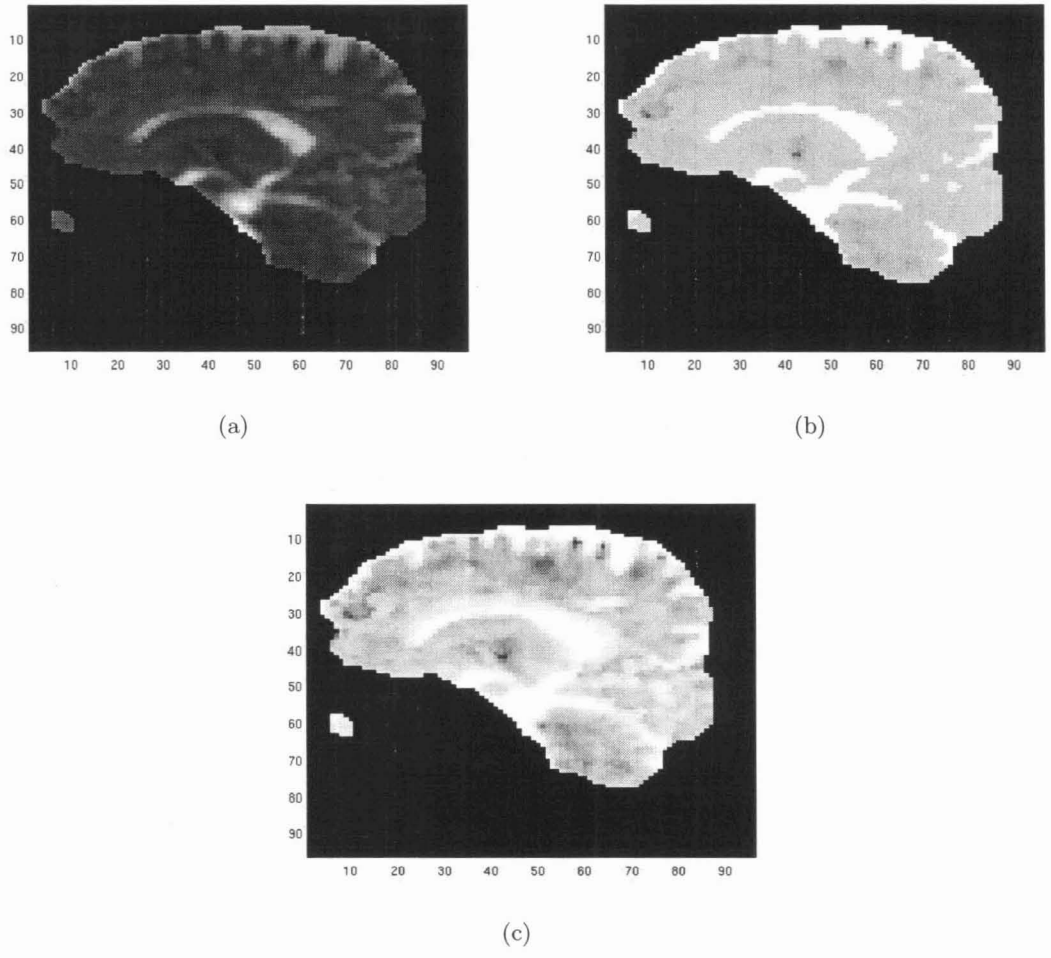

(a) (b)

(c)

Figure 6.2: (a) Apparent diffusion coefficient, (b) Fractional anisotropy and (c) Relative anisotropy of a brain slice data. All of them use the matlab default gray color map, which is a 64×3 matrix with values $[0, 1]$.

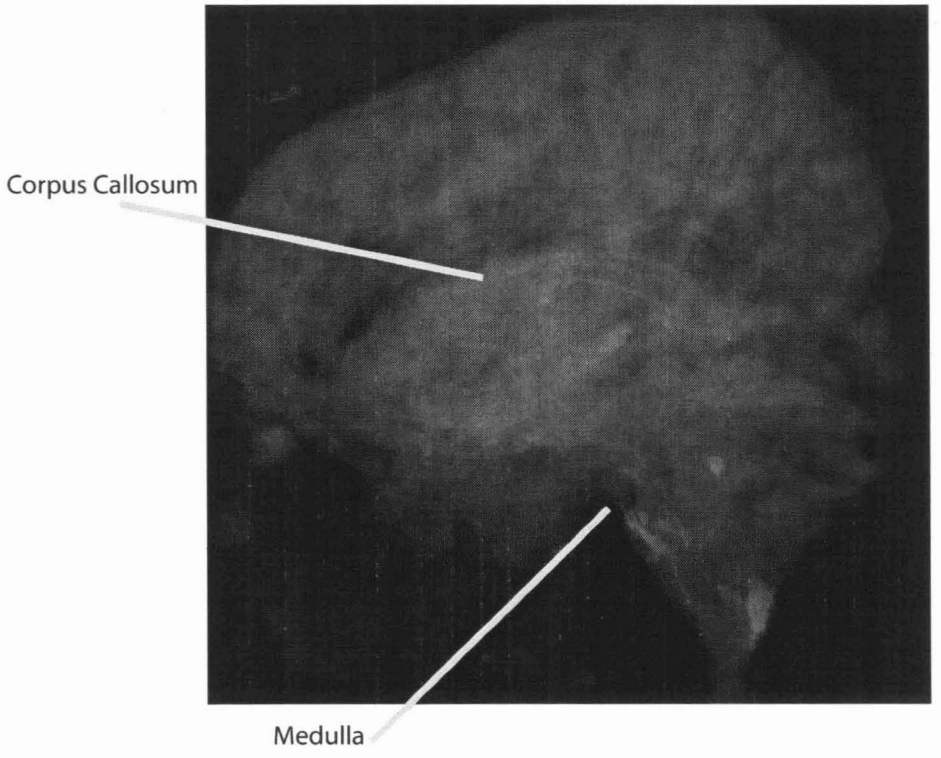

(a)

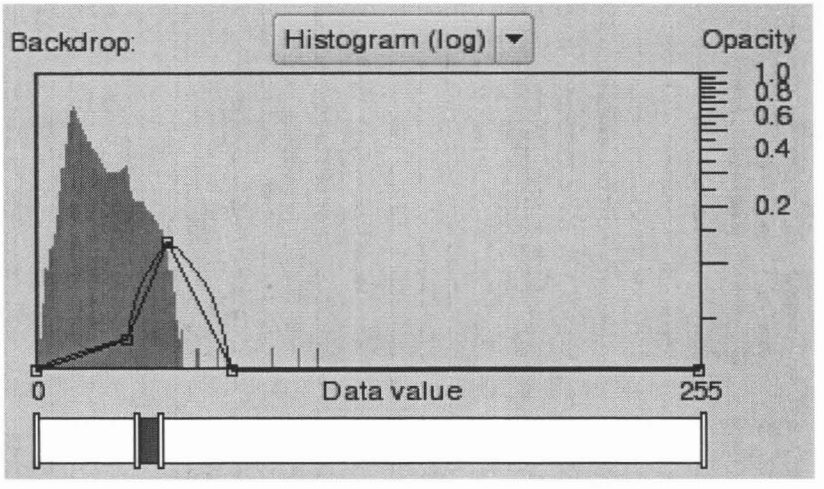

(b)

Figure 6.3: In order to highlight both corpus callosum and medulla, which are two important areas of research, a tensor in corpus callosum is chosen as the template tensor. (a) Volume rendering of Vemuri's distance to the template tensor at (40, 60, 33), a tensor located in the corpus callosum. (b) Corresponding transfer function assignment.

Chapter 7

Conclusions

We propose several new analysis and visualization methods that are designed to help the user effectively explore time-varying medical image data sets. All our methods are based on an analysis of temporal information (TAC) associated with the dynamic data. This is different from previous visualization methods [67]. We apply three similarity measures between different TACs and base our visualizations on them. We find that the maximum correlation is robust under noise, which is important for nuclear medical imaging data which often have high noise and thus low statistics. However, this similarity metric is not well suited for taking into account the Euclidian distance. We find the Euclidian distance to be an important instrument to differentiate between tissues with the same temporal behaviour but belonging to different, spatially separated organs.

We propose three principle approaches for the exploration of time-varying data: using a 1D TAC distance histogram; a 2D geometric vs. a TAC distance histogram; and the 2D layout of spring mass based clustering. The first two methods are fast and intuitive. However, they require the user to have some previous knowledge about the underlying data in order to choose the proper template TAC. The third method does not require such a template TAC and provides an overview of the complete data set. It takes, however, much longer to create such a layout. We use multi-dimensional scaling to lay out the whole data set as a backdrop for specifying a 2D transfer function. Our interface provides flexibility to the user and can be a powerful tool for gaining understanding of time-varying data. To the best of our knowledge, no similar work has been proposed before.

Another part of our work is DT-MRI visualization. The user first chooses a tensor as a template. We then apply the distance metric, proposed by Vemuri et. al. [73], between

the template tensor and all other tensors in the DT-MRI. Direct volume rendering is used to visualize the resulting scaler volume, which represents the similarity between template tensor and all other tensors. This visualization method could clearly show the region similar or dissimilar to our template tensor.

Chapter 8

Future Work

The purpose of the tool we have developed is not clinical use. Typically in the daily clinical routine there is no time to specify transfer functions etc. Therefore, our tool is more intended for use by a researcher, a medical physicist, for example, who is involved in the development of new dynamic reconstruction and analysis algorithms or investigation of new tracers. While the ideas presented in this thesis work have been developed and tested in collaboration with such a physicist, at this point we have only applied them to simulated data created for research purposes and to one dynamic planar image.

- At the next stage, we plan to extend these tests to several different types of clinical data and to involve our medical collaborators in the assessment and optimization of the method.

- Further, it presently takes too long to compute the MDS layout (several hours for a 64^3 dataset). We are actively collaborating with the creators of MDSteer [79] to incorporate into our program the next version of their system, called Glimmer, which is implemented on a modern graphics processing unit (GPU) and is faster by several orders of magnitudes than the current version.

- Currently, the distance metrics between TACs are limited to several pre-defined choices. We believe that different distance metrics should apply to different medical imaging modalities. The clinical parameters will be explored in order to capture the important features of different modalities. We will collaborate with experts of different medical modalities to explore meaningful metrics.

- The "distance" measurement between the template tensor is used to generate the distance volume. In the next stage, we will extend the MDSteer layout framework for visualizing time-varying medical data sets to DTI visualization.

Bibliography

[1] P. Acton, L. Pilowsky, D. Costa, and P. Ell. Multivariate Cluster Analysis of Dynamic Iodine-123 Iodobenzamide SPET Dopamine D_2 Receptor Images in Schizophrenia. In *European Journal of Nuclear Medicine*, pages 111–118, 1997.

[2] P. Acton, L. Pilowsky, H. Kung, and P. Ell. Automatic segmentation of dynamic neuroreceptor single-photon emission tomography images using fuzzy clustering. In *European journal of nuclear medicine*, pages 581–90, 1999.

[3] Hiroshi Akiba, Nathaniel Fout, and Kwan-Liu Ma. Simultaneous classification of time-varying volume data based on the time histogram. In *Proc. of EuroVis 2006*, 2006.

[4] D. Alexander, C. Pierpaoli, P. Basser, and J. Gee. Spatial transformations of diffusion tensor magnetic resonance images. In *IEEE Trans. Med. Imag. Anal.*, volume 20, pages 1131–1139, 2001.

[5] Daniel Alexander, James Gee, and Ruzena Bajcsy. Similarity measure for matching diffusion tensor images. In *British Machine Vision Conference 99*, pages 93–102, 1999.

[6] Nina Amenta and Jeff Klingner. Case study: Visualizing sets of evolutionary trees. In *IEEE Symposium on Information Visualization*, pages 71–74, 2002.

[7] Biosignal Analysis and Medical Imaging Group. `http://bsamig.uku.fi/research/dynspect.shtml`.

[8] Principal Components Analysis. `http://en.wikipedia.org/wiki/Principal_components_analysis`.

[9] Chandrajit L. Bajaj, Valerio Pascucci, and Daniel R. Schikore. The contour spectrum. In *Proceedings of the 8th IEEE Conference on Visualization '97*, pages 167–175. IEEE Computer Society Press, 1997.

[10] P. J. Basser, J. Mattiello, and D. LeBihan. Microstructural features measured using diffusion tensor imaging. In *Jounal of Magnetic Resanonce, Series B*, pages 209–219, 1996.

[11] P. J. Basser, S. Pajevic, C. Piperpaoli, J. Duda, and A. Aldroubi. *In vivo* fiber tractorgraphy using DT-MRI data. In *Magnetic Resonance in Medicine*, pages 44:625–632, 2000.

[12] M. Bjornemo, A. Brun, R. Kikinis, and C.-F. Westin. Regularized Stochastic White Matter Tractography Using Diffusion Tensor MRI. In *Medical Image Computing and Computer-Assisted Intervention*, 2002.

[13] I. Borg and P. J. F. Groenen. *Modern Multidimensional Scaling Theory and Applications.* Springer-Verlag, 1997.

[14] B. Burgeth, M. Welk, C. Feddern, and J. Weickert. Morphological operations on matrix-valued images. In *Computer Vision, ser. Lecture Notes in Computer Science*, volume 3024, pages 155–167, 2004.

[15] Pierpaoli C and P. J. Basser. Toward a quantitative assessment of diffusion anisotropy. In *Magn. Reson. Med.*, pages 36(6):893–906, 1996.

[16] V. Caselles, R. Kimmel, and G. Sapiro. Geodesic active contour. In *International Conference on Computer Vision*, pages 694–699, 1995.

[17] Matthew Chalmers. A linear iteration time layout algorithm for visualising high-dimensional data. In *IEEE Visualization*, pages 127–132, 1996.

[18] Raghavendra Chandrashekara, Daniel Rueckert, and Raad Mohiaddin. Cardiac Motion Tracking in Tagged MR Images Using a 4D B-spline Motion Model and Nonrigid Image Registration. In *ISBI*, pages 468–471, 2004.

[19] C. Chefd'hotel, O. Faugeras, D. Tschumperl, and R. Deriche. Constrained flows of matrix-valued functions: Application to diffusion tensor regularization. In *European Conference on Computer Vision*, pages 251–265, 2002.

[20] Jun Chen, Steve Gunn, Mark Nixon, Roger Gunn, Michael Insana, and Richard Leahy. Markov Random Field Models for Segmentation of PET Images. In *17th International Conference on Information Processing in Medical Imaging*, pages 81–92, 2001.

[21] H. Doleisch, M. Mayer, M. Gasser, R. Wanker, and H. Hauser. Case study: Visual analysis of complex, time-dependent simulation results of a diesel exhaust system. In *In Proc. of the 6th Joint IEEE TCVG - EUROGRAPHICS Symposium on Visualization*, pages 91–96, 2004.

[22] Helmut Doleisch, Martin Gasser, and Helwig Hauser. Interactive feature specification for focus+context visualization of complex simulation data. In *VISSYM '03: Proceedings of the Symposium on Data Visualisation 2003*, pages 239–248, Aire-la-Ville, Switzerland, Switzerland, 2003. Eurographics Association.

[23] C. Feddern, J. Weickert, and B. Burgeth. Level-set methods for tensor-valued images. In *Proc. of the IEEE 2nd workshop on Variational and Level Set Methods*, pages 65–72, 2003.

[24] K. Friston, A. Holmes, K. Worsley, J. Poline, C. Frith, and R. Frackowiak. Statistical Parametric Maps in Functional Imaging: A General Linear Approach. In *Human Brain Mapping*, pages 189–210, 1995.

[25] Medical Imaging Research Group. `http://www.phas.ubc.ca/~mirg`.

[26] Hongbin Guo, Rosemary Renaut, Kewei Chen, and Eric Reiman. Clustering huge data sets for parametric PET imaging. In *Biosystems*, pages 81–92, 2003.

[27] Stefan Guthe and Wolfgang Straßer. Real-time decompression and visualization of animated volume data. In *IEEE Visualization 2001 Conference*, 2001.

[28] L. Ibanez and W. Schroeder. *ITK Software Guide: The Insight Segmentation and Registration Toolkit.* Kitware Inc., 2005.

[29] Diffusion Weighted Imaging. `http://en.wikipedia.org/wiki/Diffusion-weighted_imaging`.

[30] T.J. Jankun-Kelly and Kwan-Liu Ma. A study of transfer functions generation for time-varying volume data. In *Proceedings of the Joint IEEE TCVG and Eurographics Workshop on Volume Graphics 2001*, pages 51–68, 2001.

[31] W. Kerwin, N. Osman, and J. Prince. Image Processing and Analysis in Tagged Cardiac MRI. In *Handbook of Medical Imaging*, pages 375–391, 2000.

[32] G. Kindlmann, D. Weinstein, and D. A. Hart. Strategies for direct volume rendering of diffusion tensor fields. In *IEEE Transactions on Viusalization and Computer Graphics*, pages 6(2):124–138, 2000.

[33] Gordon Kindlmann. Superquadric tensor glyphs. In *Proceedings of IEEE TVCG/EG Symposium on Visualization 2004*, pages 147–154, May 2004.

[34] P. Kingsley. Introduction to diffusion tensor imaging mathematics. In *Concepts in Magnetic Resonance Part A*, volume 28A, pages 101–122, 2006.

[35] Timo Kohlberger, Daniel Cremers, Mikaël Rousson, Ramamani Ramaraj, and Gareth Funka-Lea. 4D Shape Priors for a Level Set Segmentation of the Left Myocardium in SPECT Sequences. In *MICCAI (1)*, pages 92–100, 2006.

[36] Heidi Koivistoinen, Jussi Tohka, and Ulla Ruotsalainen. Comparison of Pattern Classification Methods in Segmentation of Dynamic PET Brain Images. In *Signal Processing Symposium*, pages 73–76, 2004.

[37] David H. Laidlaw, Eric T. Ahrens, David Kremers, and Carol Readhead. Visualizaing diffusion tensor images of the mouse spinal cord. In *Proceedings of IEEE Visualizaton 1998*, pages 127–134, 1998.

[38] Marc Levoy. Display of surfaces from volume data. In *IEEE Computer Graphics and Applications*, volume 8, pages 29–37, 1988.

[39] Kang-Ping Lin, Shyhliang A. Lou, Chin-Lung Yu, Being-Tau Chung, Liang-Chi Wu, and Ren-Shyan Liu. Markov random field method for dynamic PET image segmentation. *Medical Imaging 1998: Image Processing*, 3338(1):1198–1204, 1998.

[40] Fisher's linear Discriminat. `http://en.wikipedia.org/wiki/Linear_discriminant_analysis`.

[41] Lars Linsen, Valerio Pascucci, Mark A. Duchaineau, Bernd Hamann, Kenneth I. Joy, S. Coquillart, H.-Y. Shum, and S.-M. Hu. Hierarchical Representation of Time-varying Volume Data with 4th-root-of-2 Subdivision and Quadrilinear B-spline Wavelets. In *Proc. of Tenth Pacific Conference on Computer Graphics and Applications - Pacific Graphics*, page 346, 2002.

[42] Eric Lum, Kwan-Liu Ma, and John Clyne. Texture hardware assisted rendering of time-varying volume data. In *Proc. of IEEE Visualization 2001*, 2001.

[43] B. Burgeth M. Welk, C. Feddern and J. Weickert. Median filtering of tensor-valued images. In *Pattern Recognition, ser. Lecture Notes in Computer Science*, volume 2781, pages 17–24, 2007.

[44] Kwan Liu Ma and Eric B. Lum. Techniques for visualizing time-varying volume data. In *The Visualization Handbook*, pages 511–531, 2005.

[45] R. Mallad, J. A. Sethian, and B. C. Vemuri. Shape modeling with front propagation: A level set approach. In *IEEE Trasactions on Pattern Analysis and Machine Intelligence 17(2)*, pages 158–175, 1995.

[46] T. McInerney and D. Terzopoulos. A dynamic finite element surface model for segmentation and tracking in multidimensional medical images with application to cardiac 4D image analysis. *IEEE Transactions on Computerized Medical Imaging and Graphics*, pages 69–83, 1994.

[47] D. Metaxas, T. Chen, X. Huang, and L. Axel. Cardiac Segmentation from MRI-Tagged and CT Images. In *International Conf. on Computers, special session on Imaging and Image Processing of Dynamic Processes in biology and medici*, 2004.

[48] A. A. Mirin, R. H. Cohen, B. C. Curtis, W. P. Dannevik, A. M. Dimits, M. A. Duchauneau, D. E. Eliason, D. R. Schikore, S. E. Anderson, D. H. Porter, P. R. Woodward, L. J. Shieh, and S. W. White. Very High Resolution Simulation of Compressible

Turbulence on the IBM-SP System. In *ACM/IEEE Supercomputing 1999 Conference (SC'99)*, page 70, Los Alamitos, CA, USA, 1999. IEEE Computer Society.

[49] Johan Montagnat and Herve Delingette. Space and Time Shape Constrained Deformable Surfaces for 4D Medical Image Segmentation. In *MICCAI '00: Proceedings of the Third International Conference on Medical Image Computing and Computer-Assisted Intervention*, pages 196–205, London, UK, 2000. Springer-Verlag.

[50] Alistair Morrison, Greg Ross, and Matthew Chalmers. A hybrid layout algorithm for sub-quadratic multidimensional scaling. In *Proc. IEEE Information Visualization*, pages 152–158, 2002.

[51] Alistair Morrison, Greg Ross, and Matthew Chalmers. Fast multidimensional scaling through sampling. In *Proc. IEEE Information Visualization*, pages 68–77, 2003.

[52] J. Mattiello P. Basser and D. LeBihan. Estimation of the effective self-diffusion tensor from the NMR spin echo. In *J. Magn. Res. B*, volume 103, pages 247–54, 1994.

[53] Vladimir Pekar, Rafael Wiemker, and Daniel Hempel. Fast detection of meaningful isosurfaces for volume data visualization. In *Proceedings of the IEEE Conference on Visualization '01*, pages 223–230. IEEE Computer Society, 2001.

[54] Frits H. Post, Benjamin Vrolijk, Helwig Hauser, Robert S. Laramee, and Helmut Doleisch. The state of the art in flow visualization: feature extraction and tracking. In *Computer Graphics Forum, Vol. 22, No. 4*, pages 775–792, 2003.

[55] Dimension Reduction. `http://en.wikipedia.org/wiki/Dimensionality_reduction`.

[56] A. Reilhac, G. Batan, C. Michel, C. Grova, J. Tohka, N. Costes, and A. C. Evans. PET-SORTEO: validation and development of database of Simulated PET volumes. In *IEEE Trans. Nucl. Sci., 2004*, pages 1321– 1328, 2004.

[57] Freek Reinders, Frits H. Post, and Hans J. W. Spoelder. Visualization of time-dependent data with feature tracking and event detection. In *The Visual Computer*, pages 55–71, 2001.

[58] J. Ruiz-Alzola, C. F. Westin, S. K. Warfield, C. Alberola, S. E. Maier, and R. Kikinis. Nonrigid registration of 3-D tensor medical data. In *Med. Image Anal.*, volume 6, pages 143–161, 2002.

[59] Han-Wei Shen, Ling-Jan Chiang, and Kwan-Liu Ma. A fast volume rendering algorithm for time-varying fields using a time-space partitioning (TSP) tree. In *IEEE Visualization '99*, pages 371–378, 1999.

[60] Martha E. Shenton, Marek Kubicki, and Robert W. McCarley. Diffusion tensor imaging: Image acquisition and processing tools. In *Surgical Planning Laboratory, Technical Report #354*, 2002.

[61] D. Silver and X. Wang. Tracking and Visualizing Turbulent 3D Features. In *IEEE Transactions on Visualization and Computer Graphics*, pages 129–141, 1997.

[62] Ting Song, Vivian S. Lee, Henry Rusinek, Samson Wong, and Andrew F. Laine. Integrated Four Dimensional Registration and Segmentation of Dynamic Renal MR Images. In *MICCAI (2)*, pages 758–765, 2006.

[63] E. O. Stejskal and J. E. Tanner. Spin diffusion measurements: Spin echos in the presence of a time-dependent field gradient. In *J. Chem. Phys.*, volume 42, pages 288–292, 1965.

[64] Philip Sutton and Charles D. Hansen. Isosurface extraction in time-varying fields using a temporal branch-on-need tree (T-BON). In *Proceedings of IEEE Visualization '99*, pages 147–153, 1999.

[65] Klaus D. Toennies, Anna Celler, Stephan Blinder, and Ronald Harrop Torsten Möller. Scatter Segmentation in Dynamic SPECT Images usign Principal Component Analysis. In *Proc. of SPIE International Symposium on Medical Imaging*, pages 507–516, 2003.

[66] Positron Emission Tomography. `http://en.wikipedia.org/wiki/Positron_emission_tomography`.

[67] Melanie Troy, Niklas Röber, Torsten Möller, Anna Celler, and M. Stella Atkins. 4D Space-Time Technique: A Medical Imaging Case Study. In *Proc. IEEE Visualization 2001*, pages 473–476, 2001.

[68] A. Tsai, A. Yezzi Jr., and A. S. Willsky. Curve Evolution Implementation of The Mumford-shah Functional for Image Segmentation, Denoising, Interpolation, and Magnification. In *TIP*, pages 10(8):1169–1186, Aug. 2001.

[69] K. Tsuda, S. Akaho, and K. Asai. The em Algorithm for Kernel Matrix Completion with Auxiliary Data. In *Journal of Machine Learning Research*, pages 4:67–81, 2003.

[70] B.M. Tsui, J.A. Terry, and G.T. Gullberg. Evaluation of cardiac cone-beam SPECT using observer performance experiments and ROC analysis. *Investigative Radiology*, 28(12):1101–1112, July 1993.

[71] Fan-Yin Tzeng and Kwan-Liu Ma. Intelligent Feature Extraction and Tracking for Visualizing Large-Scale 4D Flow Simulations. In *Supercomputing, 2005. Proceedings of the ACM/IEEE SC 2005 Conference*, page 6, 2005.

[72] P. K. Velamuru, R. A. Renaut, H. Guo, and K. Chen. Robust clustering of positron emission tomography data. In *Joint Conference of the Classification Society of North America and Interface Foundation of North America*, 2005.

[73] Zhizhou Wang and Baba C. Vemuri. An affine invariant tensor dissimilarity measure and its applications to tensor-valued image segmentation. In *Computer Vision and Pattern Recognition, vol. 1*, pages 228–233, 2004.

[74] Joachim Weickert. Diffusion and regularization methods for tensor-valued images. In *First SIAM-EMS Conference: Applied Mathematics in Our Changing World*, 2001.

[75] D. M. Weinstein, G. L. Kindlmann, and E. C. Lundberg. Tensorlines: Advection diffusion-based propagation through diffusion tensor fields. In *IEEE Visualization '99*, pages 249–254, 1999.

[76] Miles N. Wernick and John N. Aarsvold. Introduction to emission tomography. In *Emission Tomography: The Fundamentals of PET and SPECT*, pages 13–23, 2004.

[77] C. F. Westin, S. E. Maier, H. Mamata, A. Nabavi, F. A. Jolesz, and R. Kikinis. Processing and Visualization of Diffusion Tensor MRI. In *Medical Image Analysis*, pages 6:93–108, 2002.

[78] Jane Wilhelms and Allen Van Gelder. Octrees for faster isosurface generation. In *ACM Transactions on Graphics*, pages 201–227, 1992.

[79] Matt Williams and Tamara Munzner. Steerable, progressive multidimensional scaling. In *Proc. IEEE Information Visualization 2004*, pages 57–64, 2004.

[80] K. P. Wong, D. Feng, S. R. Meikle, and M. J. Fulham. Segmentation of Dynamic PET Images Using Cluster Analysis. In *IEEE Transactions on Nuclear Science*, pages 200–207, 2002.

[81] Jonathan Woodring, Chaoli Wang, and Han Wei Shen. High dimensional direct rendering of time-varying volumes. In *IEEE Visualization 2003*, pages 417–424, 2003.

[82] R. Xue, P. C. Van Zijl, B. J. Crain, M. Solaiyappan, and S. Mori. *In vivo* 3D Reconstruction of Rat Brain Axonal Projectings by Diffusion Tensor Imaging. In *Magn. Reson. Med.*, pages 42:1123–1127, 1999.

[83] Hamid Younesy, Torsten Möller, and Hamish Carr. Visualization of time-varying volumetric data using differential time-histogram table. In *Workshop on Volume Graphics 2005*, pages 21–29, 2005.

[84] S. Zhang, C. Demiralp, and D. H. Lailaw. Visualizing Diffusion Tensor MR Images Uing Streamtubes and Streamsurfaces. In *IEEE Transactions on Visualization and Computer Graphics*, pages 9(4):454–462, 2003.

[85] Song Zhang, David H. Laidlaw, and Gordon Kindlmann. Diffusion Tensor MRI Visualization. In *The Visualization Handbook*, pages 327–340, 2005.

[86] L. Zhukov and A. Barr. Oriented Tensor Reconstruction: Tracing Neural Pathways from Diffusion Tensor MRI. In *IEEE Conference on Visualization '02*, pages 387–394, 2002.

[87] L. Zhukov, K. Museth, D. Breen, R. Whitaker, and A. Barr. Level Set Modeling and Segmentation of DT-MRI Brain Data. In *Journal of Electronic Imaging*, pages 12(1):125–133, 2003.